การขจัดหมู่ออกซิเจนของกรดปาล์มิติกบนตัวเร่งปฏิกิริยาโลหะผสมซีเรียมออกไซด์

DEOXYGENATION OF PALMITIC ACID OVER CERIUM - METAL OXIDE

นางสาวชาลินี ตารารัตน์

นายธีรพงษ์ กุลรัตน์

นายชูเชษฐ์ สุนทรทวีทรัพย์

โครงงานนี้เป็นส่วนหนึ่งของการศึกษาตามหลักสูตรวิทยาศาสตรบัณฑิต

สาขาวิชาเคมีอุตสาหกรรม

คณะวิทยาศาสตร์

สถาบันเทคโนโลยีพระจอมเกล้าเจ้าคุณทหารลาดกระบัง

ปีการศึกษา 2556

การขจัดหมู่ออกซิเจนของกรดปาล์มิติกบนตัวเร่งปฏิกิริยาโลหะผสมซีเรียมออกไซด์

DEOXYGENATION OF PALMITIC ACID OVER CERIUM-METAL OXIDE

นางสาวชาลินี ดารารัตน์

นายธีรพงษ์ กุลรัตน์

นายสุรเชษฐ์ สุนทรทวีทรัพย์

โครงงานพิเศษนี้เป็นส่วนหนึ่งของการศึกษาตามหลักสูตรวิทยาศาสตรบัณฑิต

สาขาวิชา เคมีอุตสาหกรรม

คณะวิทยาศาสตร์

สถาบันเทคโนโลยีพระจอมเกล้าเจ้าคุณทหารลาดกระบัง

ปีการศึกษา 2556

DEOXYGENATION OF PALMITIC ACID OVER CERIUM-METAL OXIDE

Miss CHALINEE DARARAT

Mr. TEERAPONG KULRAT

Mr. SURACHET SOONTONTAWEESUB

A SPECIAL PROJECT SUBMITTED IN PARTIAL FULFILLMENT

OF THE REQUIREMENT FOR THE DEGREE OF BACHELOR OF SCIENCE

IN INDUSTRIAL CHEMISTRY

FACULTY OF SCIENCE

KING MONGKUT'S INSTITUTE OF TECHNOLOGY LADKRABANG

ACADEMIC YEAR 2013

Special project	Deoxygenation of palmitic acid over cerium-metal mixed oxide catalysts
Student	Ms. Chalinee Dararat ID 53050206
	Mr. Teerapong Kulrat ID 53050245
	Mr. Surachet Soontontaweesub ID 53050386
Degree	Bachelor of Science
Program	Industrial chemistry
Year	2013
Thesis Adviser	Assoc. Prof. Dr. Tawan Sooknoi
	Dr. Tosapol Maluangnont

Faculty of Science, King Mongkut's Institute of Technology Ladkrabang, has approved this special project submitted in partial fulfillment of the requirement for the degree of Bachelor of Science in academic year 2013.

Committees	Signatures
Asst. Prof. Dr Sutha Sutthiruangwong	
Asst. Prof. Dr. Montree Thongkam	
Assoc. Prof. Dr. Tawan Sooknoi	
Dr. Tosapol Maluangnont	

Special project	Deoxygenation of palmitic acid over cerium-metal mixed oxide catalysts	
Student	Ms. Chalinee Dararat	ID 53050206
	Mr. Teerapong Kulrat	ID 53050245
	Mr. Surachet Soontontaweesub	ID 53050386
Degree	Bachelor of Science	
Program	Industrial chemistry	
Adviser	Assoc. Prof. Dr. Tawan Sooknoi	
Co-Adviser	Dr. Tosapol Maluangnont	

ABSTRACT

In this thesis, the decarboxylation of palmitic acid to produce linear alpha olefins (LAOs) over ceria catalyst and cerium-metal mixed oxide catalysts, were investigated. The XRD pattern of all catalyst showed cubic fluorite structure. CeO_2 synthesized by a surfactant-assisted method has BET surface area (159 m^2/g) higher than other catalysts prepared by conventional co-precipitation method. The reduction of cerium oxide and cerium-metal mixed oxide catalyst is investigated by Temperature Program Reduction (TPR). Raman spectroscopy was employed to study the presence of oxygen vacancy in the catalysts; it showed that $Ce_{0.5}Zr_{0.5}O_2$ has the largest concentration of oxygen vacancy as seen by the broad band at 550-650 cm^{-1}. Catalytic activity testing showed that palmitic acid was converted to C_{31} ketone via ketonization. This ketone can undergo cracking to C_{17} ketone, heavy ketone/alcohol and hydrocarbons including liquid and smaller hydrocarbons. Under hydrogen flow, C_{17} ketone can be hydrogenated to C_{17} alcohol and further dehydrated to C_{17} unsaturated hydrocarbon. Alternatively, palmitic acid can be reduced by oxygen vacancy to C_{16} aldehyde, which underwent subsequent hydrogenation to C_{16} alcohol and hydrogenolysis to C_{16} saturated hydrocarbon. For the reaction over non-reduced catalyst, palmitic acid can be decomposed on ceria surface to cracked acid where oxygen vacancy was generated.

Keywords: oxygen vacancy, deoxygenation, ketonization, ceria, cerium oxide, palmitic acid.

ACKNOWLEDGEMENTS

For the thesis completion, we would gratefully like to thank our advisor, Assoc. Prof. Dr. Tawan Sooknoi for his supports, supervisions, inspiration, suggestions and encouragements throughout this thesis. Also, we wish also to thank Dr. Tosapol Maluangnont for his stimulating suggestions and encouragement in research in inorganic chemistry and material science. Our acknowledgement extends to Dr. Nutthida Numwong for her advices, suggestion and kindness.

We thank Asst. Prof. Dr. Sutha sutthiruangwong and Asst. Prof. Dr. Montree Thongkam for serving on the committee and for their valuable comments.

We also appreciate the supports from the Department of Chemistry, Faculty of Science, King Mongkut's Institute of Technology Ladkrabang for the equipments, chemicals and facilities.

We would like to extend our sincere appreciation to all teachers, friends and members of the research group for their constant guidance advice, support and encouragement.

Finally, we deeply appreciate and thank our family for their love and supports.

CHALINEE DARARAT

TEERAPONG KULRAT

SURACHET SOONTONTAWEESUB

TABLE OF CONTENTS

TABLE OF CONTENTS (Continued)

TABLE OF CONTENTS (Continued)

LIST OF TABLES

LIST OF FIGURES

LIST OF FIGURES (Continued)

APPENDIX

LIST OF FIGURES (Continued)

CHAPTER 1

INTRODUCTION

1.1 Motivation

Nowadays, the increasing fuel and chemical consumption has led to a rapid depletion of fossil feedstock. Biomass has therefore become a potential candidate as renewable feedstock for fuels and chemicals. This aspect is particularly interesting for an agricultural country like Thailand.

One of the important chemical feedstock that can be derived from biomass is linear alpha olefins (LAOs). They are widely used for plasticizer, lubricant, surfactant, etc. LAOs are traditionally produced from an oligomerization of ethylene [1], which is a non-renewable feedstock. An alternative approach for the synthesis of LAOs is via the decarbonylation of fatty acids. Fatty acids, which are considered as the derivative of the biomass, can be easily obtained from a hydrolysis of triglycerides from vegetable oils and animals fats.

In order to make LAOs from fatty acids, the oxygen atoms (i.e., the carboxylic group) need to be removed, usually with help of a catalyst with basic functionality. The carboxylic group will be absorbed on the surface of a catalyst, and a metal carboxylate salt is formed. The salt can be decomposed to *alkane* and carbon dioxide at high temperature by the pathway shown in equation (1.1.) This reaction, which is called "decarboxylation", is however not economically attractive, as alkane molecules can also be made by other processes at milder conditions than those of the decarboxylation.

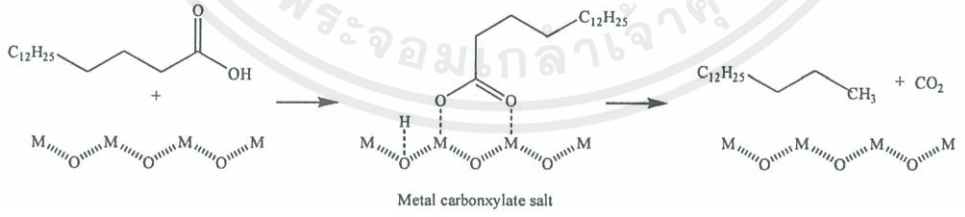

(1.1)

Apart from that, the removal of carboxylic group can occur via "decarbonylation", yielding alkenes as a product. Generally, this reaction requires a metal oxide catalyst with high lattice energy. The oxygen vacancy (Ov) in the lattice of the catalyst will interact with the oxygen atom at the carboxylic group as shown in equation (1.2.) The subsequent step is the loss of the beta-hydrogen, that is, a hydrogen atom attached to a carbon atom two positions away from the

carboxylic group. Consequently, carbon monoxide and water are produced together with an alkene with the double bond at the 1 (or alpha)-position. The alkenes are more valuable than alkanes.

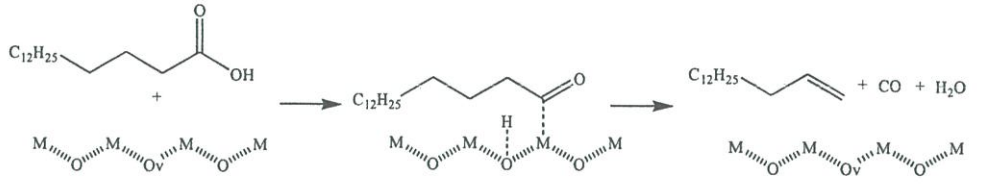

(1.2)

Unfortunately, the high selectivity towards LAOs is low due to their tendency to undergo isomerization, which ultimately leads to internal alkenes. Besides, the decarboxylation to alkanes can also occur as the side reaction under the experimental conditions where decarbonylation is operative. The removal of oxygen atoms is called collectively as "deoxygenation".

Cerium (IV) oxide, also known as ceria (CeO_2) is well known for its ability to accommodate oxygen vacancies on its surface [2]. This behavior is heavily utilized in reactions such as catalytic wet oxidation of organic pollutants in water, or the treatment of noxious gases (e.g., NO, CO) released from engines. Herein, we propose the oxygen vacancies as the catalytically active sites for the deoxygenation of fatty acid. We will also study CeO_2 doped with other metal cations M which are capable of altering the number and/or strength of the oxygen vacancies by different mechanisms. In $Ce_{1-x}M_xO_{2-y}$ (M = Cu^{2+}, Co^{2+}), the cations whose the valency is different (2+) from Ce^{4+} [3], will induce the formation of oxygen vacancies due to charge imbalance. We will also study the case where M = Zr^{4+}, whose the valency is the same as Ce^{4+}, but the ionic radius is so different that oxygen vacancies are created through the strain in the lattice. These materials will be reduced by H_2 gas prior to the reaction, so as to gain insights into the correlation between the catalytic activity, the reducibility of the doped metal cations, and the generation of oxygen vacancies. The optimized catalytic conditions for the catalysts prepared will be investigated as well.

1.2 Objectives

1.2.1 To obtain linear alpha olefins from the deoxygenation of palmitic acid over ceria and metal-substituted ceria.

1.2.2 To understand the role of oxygen vacancies in ceria and metal-substituted ceria toward the deoxygenation.

1.3 Scope of the study

The scopes of this thesis are as follows:

1.3.1 Synthesis of ceria and metal-substituted ceria catalysts by (i) surfactant associated method and (ii) co-precipitation method.

1.3.2 Characterization of ceria and metal-substituted ceria catalysts by X-ray diffraction (XRD), temperature program reduction (TPR), Raman spectroscopy, and surface area measurement, Scanning electron microscope (SEM) and Thermogravimetric analysis (TGA).

1.3.3 Investigation on the use of ceria and metal-substituted ceria in the deoxygenation of palmitic acid in a continuous reactor.

1.3.4 Investigation on the following factors toward catalytic activity: role of oxygen vacancies and types of incorporated metal cations.

1.3.5 Analysis and quantification of products by a gas chromatography equipped with a flame ionization detector (GC-FID)

1.4 Expected results

It is expected that a new technology for the production of long chain hydrocarbons from palmitic acid will be obtained. This technology could potentially be developed into a process for alpha-olefins production from the renewable source within the country.

CHAPTER 2

THEORY AND LITERATURE REVIEWS

2.1 Fatty acids

Fatty acids refer to aliphatic monocarboxylic acids, and are one of the most important building blocks for the synthesis of fuels and chemicals on an industrial scale [4-5]. Fatty acids can be produced by the hydrolysis of triglycerides, which are major components in animal fats (e.g., butter, lard, beef), vegetable oils (e.g., jatropha oil, coconut oil, palm oil), or waxes. Natural fatty acids commonly have an unbranched chain with even number of carbon atoms (mostly 16-22) which can be either saturated or unsaturated. Saturated fatty acids do not contain any double bonds, and therefore are not capable of receiving additional number of hydrogen atoms. On the other hand, unsaturated fatty acids have at least one double bond, where hydrogen atoms can be added into. Most of the naturally-occurring unsaturated fatty acids are *cis*-isomers. The *trans*-isomers are usually not found in nature and are the result of the processing (e.g., hydrogenation).

The world production of fatty acids from the hydrolysis of natural fats and oils is about 4 million metric tons per year [6]. Fatty acids are ultimately consumed in a wide variety of end-use industries, such as rubbers, plastics, detergents. Fatty acids make up the greatest proportion for the current consumption of raw materials in the chemical industry. The extent of the chemical reactions which are used to transform these renewable materials into other fuels will be summarized in the next section, after a brief discussion on the fatty acid to be investigated.

2.1.1 Palmitic acid

Palmitic acid, $CH_3(CH_2)_{14}COOH$ or hexadecanoic acid in IUPAC nomenclature, is one of the most common saturated fatty acids found in animals and plants. It structure is shown in **Figure 2.1.** As the name implies, palmitic acid is a major component in the oils from palm tree (palm oil and kernel oil). Palmitic acids can also be found in butter, cheese, milk and meat.

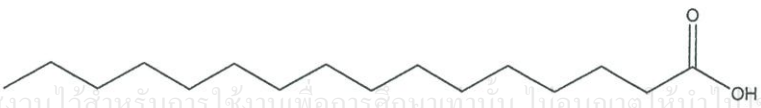

Figure 2.1 The structure of palmitic acid.

2.1.2 Reactions of fatty acids

2.1.2.1 Deoxygenation

In this context, deoxygenation is a chemical reaction involving the removal of oxygen atoms from the starting molecule [7]. It is a novel method for the production of long chain hydrocarbons (diesel, olefin) from renewable sources, and is currently being investigated worldwide. The deoxygenation can occur via decarboxylation, which involves the release of carbon dioxide gas together with alkane molecules as shown in equation (2.1).

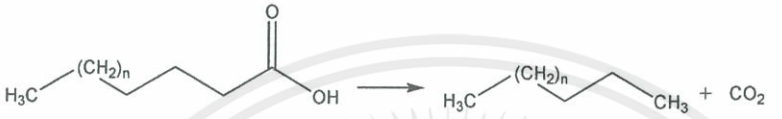

(2.1)

Alternatively, deoxygenation can occur via equation (2.2) which is known as decarbonylation, with the release of carbon monoxide, water, and alkene. Decarbonylation is more attractive than decarboxylation from the economic point of view, as alkenes are generally considered more valuable than alkanes.

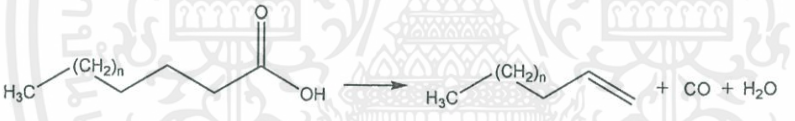

(2.2)

2.1.2.2 Ketonization

Ketonization (also known as ketonic decarboxylation) is a reaction where two equivalents of carboxylic acid are converted into a symmetric ketone, with the expulsion of one equivalent of water and carbon dioxide each as shown in equation (2.3). This reaction is catalyzed by bases. The reaction mechanism likely involves the formation of carbanions as the intermediate from the decarboxylation of one acid group, followed by a nucleophilic attack by another acid group as a concerted reaction (S_N2). This reaction is different from the oxidative decarboxylation which proceeds through a radical mechanism, and is characterized by a different product distribution in isotopic labeling experiments with two different carboxylic acids.

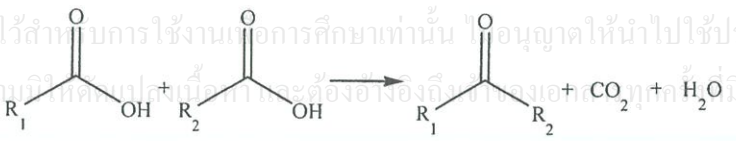

(2.3)

2.2 Metal oxide

2.2.1 Oxygen vacancies-containing catalysts

Oxygen vacancies-containg catalysts are the one where some portions of oxygen atoms on the surface are missing, hence the name vacancy. It is suggested that a diatomic species of peroxide ion (O_2^{2-}) is an active species on the surfacc [8]. The vacancies as the defects can be rapidly formed and eliminated, depending on environmental conditions where the catalysts are employed.

This phenomenon is known as "oxygen storage capacity", and is exploited in e.g., the complete/partial oxidation, or the treatment of harmful gas released from the incomplete combustion of engines. Examples for common oxides known to contain oxygen vacancies are CeO_2 and ZrO_2. Materials based on CeO_2 will be the subject of this work.

2.2.1.1 Ceria

Cerium (IV) oxide (also known as ceria oxide, ceria, cerium oxide or cerium dioxide) is a pale yellow-white powder with the chemical formula CeO_2, where the nominal oxidation state of cerium is 4+ [9]. Cerium (IV) oxide is the most stable oxides of cerium under room temperature and atmospheric conditions. It can be made by heating cerium oxalate or cerium hydroxide at high temperature in air. Powdered ceria is slightly hygroscopic and will also absorb a small amount of carbon dioxide from the atmosphere.

Cerium (IV) oxide has the fluorite structure, where Ce^{4+} can be considered as forming a cubic close packed array, and O^{2-} fill all the available tetrahedral sites as shown in Figure 2.2. As all oxygen atoms are in a plane with one another, a rapid diffusion of oxygen (assuming the presence of oxygen vacancies) around the crystals is allowed. Additionally, ceria has excellent redox properties owing to the very fast reduction of Ce^{4+} to Ce^{3+} associated with the formation of oxygen vacancies at the surface and in the solids. This gives rise to the utilization of ceria as an oxidation catalyst. The catalyst surfaces with high basicity lead to the adsorption and activation of carbon dioxide to produce oxygen active species [10]. It has been shown that the catalytic activity of ceria is directly related to the number of oxygen vacancies in the crystal [11]. The amount of oxygen vacancies can be measured using X-Ray Photoelectron Spectroscopy (XPS) by examining the ratios of Ce^{3+} to Ce^{4+} in the crystals.

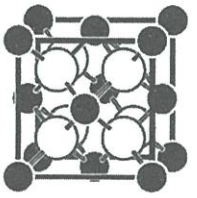

Figure 2.2 The fluorite structure of ceria: black, Ce^{4+}; white O^{2-} [11].

2.2.1.2 Metal-substituted ceria

In general, metal-substituted ceria with di or trivalent cations results in a change in the lattice parameter as compared to ceria. Consider a case where the M^{2+} is substituted to the sites of Ce^{4+}. For every M^{2+} cation that substitutes for Ce^{4+}, there will be a deficiency of two positive charges (or alternatively, an excess of two negative charges). One way to preserve charge neutrality is via the transformation of Ce^{4+} to Ce^{3+} for every 0.5 unit of M^{2+}. Such transformation generally results in the increase of the lattice constant, because the ionic radius of Ce^{3+} is larger than that of Ce^{4+}. In addition to the reduction of Ce^{4+} to Ce^{3+}, the material could regain charge neutrality if an oxygen ions O^{2-} leaves the lattices; one such a vacancy will contribute to a nominal reduction of two negative charges.

2.2.2 Method of synthesis

Co-precipitation is the process where the different cations are precipitated together under the same experimental conditions. The solids synthesized from the co-precipitation of two cations might have one type of cation substituted for another cation at certain position in the crystal structure of a solid. Co-precipitation (and the resulting inclusion into the crystal structure) usually occurs if the difference in ionic radii between the two is not unacceptably large. For example, in a solution containing Ce^{4+} and Zr^{4+}, both cations will precipitate at a pH value of 9 into the mixed oxides/hydroxides. Calcination of the precipitates will result in the formation of doped CeO_2 with the composition $Ce_{1-x}Zr_xO_2$ [12]. Here, the amount of incorporated Zr (x) will depend on several factors, some of them be the relative concentration of Zr^{4+} relative to Ce^{4+} in the starting solution, the pH at which co-precipitation is to occur, the solubility product of the two cations, etc. Co-precipitation of metal cations with different valency is also possible, given the difference in cationic radii of cations is within a certain limit, and the resulting charge imbalance is brought back to neutrality by some mechanisms. One of the example is the co-precipitation of Co^{2+} [13] or Cu^{2+} [14] in a solution containing Ce^{4+}, where heating the resulting precipitates results in the substituted ceria $Ce_{1-x}Co_xO_2$ and $Ce_{1-x}Cu_xO_2$ respectively.

The co-precipitation of cations (or the precipitation of just one type of cation) can also occur in the presence of a surfactant. Here, surfactants help improving physical properties of the solid, mostly by generating porous structure and rendering high surface area. For example, high surface-area CeO_2 can be synthesized, after the aging of Ce^{3+} with cetyltrimethylammonium bromide (CTAB) as a surfactant, followed by precipitation and calcination as usual [15]. The material has the surface area of 69 m^2/g, in contrast to the value of 5 m^2/g for CeO_2 powder synthesized without surfactant.

2.3 Characterization

2.3.1 X-ray diffraction (XRD)

In XRD measurement, the sample (powder or a crystal) is placed in a holder before it is illuminated with X-rays at a fixed wavelength, and the intensity of the reflected radiation is recorded. From the diffraction angle, the inter-atomic spacing (d value, usually in Angstrom units or 10^{-8} cm) can be determined [16]. The results obtained, usually presented as the diffraction pattern (intensity *vs* 2θ) can be used to identify the phase of the materials under investigation.

2.3.1.1 Bragg's Law

Atoms in crystals interact with X-ray radiations producing interference, as if they reflect the waves. The interference occurs as a result of the orderly arrangement of atoms into planes. Let us imagine a beam of monochromatic X-rays entering a crystal with one of these planes of atoms oriented at an angle of θ as shown in **Figure 2.3**.

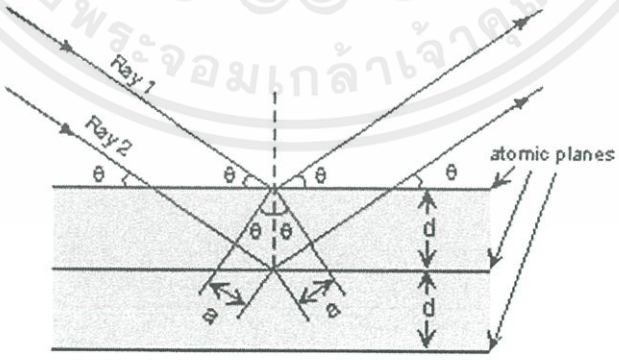

Figure 2.3 The spacing between the atomic planes [16].

For the constructive interference to take place [16],

$$n\lambda = 2a \tag{2.4}$$

The distance 2a can be transformed into the unit of the spacing, d, as

$$a = dsin\theta \tag{2.5}$$

From equation (2.4) and (2.5), we get

$$2a = 2dsin\theta \tag{2.6}$$

$$n\lambda = 2dsin\theta \tag{2.7}$$

Equation (2.7) is known as Bragg's Law for X-ray diffraction. The destructive interference will occur if the distance $2a$ is not an integral number of wavelengths, and the waves will not be as strong as when they entered the crystal. For the constructive interference, given the wavelength λ of the X-rays going in to the crystal, and the angle θ of the diffracted X-rays coming out of the crystal, the spacing between the atomic planes (referred to as d-spacing) can be calculated using equation (2.8).

$$d = \frac{n\lambda}{sin\theta} \tag{2.8}$$

It is important to point out that this diffraction will only occur if the rays are in phase when they emerge, and at the appropriate value of n (1, 2, 3, etc.) and θ.

Refining the lattice parameters of the unit cell from X-ray powder diffraction data requires the knowledge of Miller indices *hkl* for each diffraction peak, via a process known as indexing the pattern. For a known material, this can be easily done by comparing the diffraction pattern to that reported in the literature or in a database (known as the JCPDS). The Miller indices relate the peak positions or d-spacings to the lattice parameters by an equation specific to the crystal system. For example, in a cubic system such as CeO_2 (where the unit cell length $a = b = c$), equation (2.9) can be used:

$$\frac{1}{d_{hkl}^2} = \frac{h^2+k^2+l^2}{a^2} \tag{2.9}$$

2.3.1.2 Sherrer's equation

In addition to the unit cell parameter, the particle size of a material can also be calculated from XRD measurement, using Scherrer's as shown in equation (2.10):

$$D = \frac{K\lambda}{\beta cos\theta} \tag{2.10}$$

Where D = particle size, K = a constant depending on size and shape of a particle taken to be 0.9 in this work, and β = full width at half maximum (FWHM) of the peak in the unit of radians.

2.3.2 Raman spectroscopy

Raman spectroscopy is a spectroscopic technique used to observe vibrational, rotational, and other low-frequency modes in a system [17]. It relies on inelastic (or Raman) scattering of monochromatic light, usually from a laser in the visible, near infrared, or near ultraviolet range.

The laser interacts with molecular vibrations, phonons or other excitations in the system, resulting in the energy of the laser photons being shifted up or down. The shift in energy gives information about the vibrational modes in the system.

Typically, a sample is illuminated with a laser beam. Light from the illuminated spot is collected with a lens and sent through a monochromator. Wavelengths close to the laser line due to elastic Rayleigh scattering are filtered out while the rest of the collected light is dispersed onto a detector. The signal is recorded and shown as a plot of the intensity of the scattered light (on the y-axis) vs the magnitude of the shift in wavenumber of the signal relative to the starting laser in the unit of cm^{-1} (on the x-axis). The Raman spectrum can serve as a fingerprint that assists in identification of a substance, similar to the case of infrared (IR) spectroscopy. Alternatively, each peak can be ascribed to certain modes of interactions by the phonons, which is related to a crystal structure of interest including the associated symmetry.

2.3.3 Temperature program reduction (TPR)

Temperature-programmed reduction (TPR) is a widely used tool for the characterization of metal oxides, mixed metal oxides, and metal oxides dispersed on a support. This technique yields quantitative information on the reducibility of the surface of an oxide M_xO_y, including the heterogeneity of the reducible surface. In this technique, a reducing gas mixture (typically 3% to 17% of hydrogen diluted in argon or nitrogen) is fed over the sample. The sample is reduced following equation (2.11):

$$M_xO_y + yH_2 \longrightarrow xM + yH_2O \qquad (2.11)$$

A thermal conductivity detector (TCD) is used to measure changes in the thermal conductivity of the gas stream as a result of the above reaction. The TCD signal is then converted to concentration of active gas using a level calibration. Integrating the area under the concentration *vs* time (or temperature) yields the total amount of gas consumed.

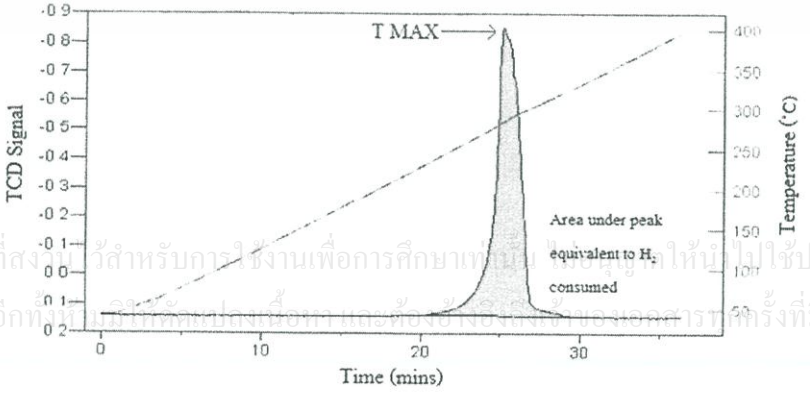

Figure 2.8 Temperature-programmed reduction (TPR) profile for a metal oxide [18].

Figure 2.8 shows a typical TPR profile for the reduction of the metal oxide M_xO_y. The peak maximum indicates the temperature corresponding to the maximum rate of the reduction. The TPR method provides a degree of reproducibility of the catalyst surface, including chemical changes resulting from promoters or metal/support interactions.

2.3.4 Surface area measurement

The specific surface area of a powder is determined by the physical adsorption of gas molecules on the surfaces, followed by a calculation of the amount of adsorbed gas which corresponds to a monolayer adsorption [19]. Physical adsorption results from relatively weak forces (van der Waals forces) between the adsorbed gas molecules and the surface area of the tested powder. The determination is usually carried out at the temperature of liquid nitrogen. The amount of gas adsorbed can be measured by a volumetric or continuous flow procedure. The surface area of the material can be calculated following an equation proposed by Brunauer–Emmett–Teller (BET) and is usually done by the software of the instrument.

2.4 Linear alpha olefins (LAOs)

The term "olefins", also known as alkenes with the empirical formula C_nH_{2n}, refers to a large number of compounds that contain carbon and hydrogen, and have at least one double bond in their structure. Short-chain olefins, e.g. ethylene, are cracked form naphtha or natural gas. Ethylene is then oligomerised into longer chain linear alpha olefins (LAOs), ranging from 6 to 30 carbons in length. Alpha olefins are characterized by their high purity, high degree of linearity, and the presence of double bond which is uniformly positioned between the first and second carbon. For drilling fluid applications, alpha olefins in the C_{14} to C_{18} range are used because they have the right mix of physical properties such as viscosity, pour point, and flash point. Internal olefins are then produced from LAOs by catalytically moving the double bond to different locations in the molecule. As a result, the pour point of the fluid decreases significantly, thus enabling these materials to be used successfully in deep-water applications. Internal olefins used as base fluids for drilling muds typically have carbons chain lengths in the C_{15} to C_{18} range [20].

2.4.1 Synthesis

2.4.1.1 Oligomerization

Ethylene-oligomerization process has been developed by Shell and is called the Shell Higher Olefin Process (SHOP) [21-23]. In this process, ethylene oligomerization is catalyzed by nickel complexes which give rise to ethylene oligomers having a Shultz-Flory distribution. The

composition of the oligomers can be adjusted to the required composition through a series of reactions combining the isomerization of the olefins with the disproportionation between the light and heavy olefins.

Alternatively, Idemitsu Kosan Co., Ltd., developed a new ethylene oligomerization process based on the catalyst consisting of $ZrCl_4$, an alkylaluminum compound, and a Lewis base; the distribution of products in this process can be adjusted by changing the ligand structure of the alkylaluminum complex [23,24].

2.4.2 Applications

There is a wide range of applications for LAOs. The lower carbon numbers such as 1-butene, 1-hexene and 1-octene are overwhelmingly used as co-monomers in the production of polyethylene. High density polyethylene (HDPE) and linear low density polyethylene (LLDPE) use approximately 2-4% and 8-10% of co-monomers, respectively.

Another significant use of C_4-C_8 LAOs is for the production of linear aldehyde via oxo synthesis (hydroformylation), for a subsequent production of short-chain fatty acid by an oxidation of an intermediate aldehyde, or linear alcohols for plasticizer application by hydrogenation of the aldehyde.

The predominant application of 1-decene is in making polyalphaolefin (PAO) synthetic lubricant basestock, and to make surfactants in a blend with higher LAOs.

C_{10}-C_{14} LAOs are used in making surfactants for aqueous detergent formulations. These carbon numbers may be reacted with benzene to make linear alkyl benzene (LAB), which is further sulfonated to linear alkyl benzene sulfonate (LABS), a popular and relatively low cost surfactant for household and industrial detergent applications.

Although some C_{14} alpha olefins are sold into aqueous detergent applications, C_{14} LAOs has other applications such as being converted into chloroparaffins, or as an on-land drilling fluid basestock, replacing diesel or kerosene in their application. Although C_{14} is more expensive than middle distillates, it is much more biodegradable, less irritating to skin, less toxic, and easier to handle.

C_{16}-C_{18} linear olefins find their primary application as the hydrophobes in oil-soluble surfactants and as lubricating fluids themselves. C_{16}-C_{18} alpha (or internal) olefins are used as synthetic drilling fluid base for high value, primarily off-shore synthetic drilling fluids. The preferred materials for the synthetic drilling fluid application are linear internal olefins, which are primarily made by isomerizing LAOs to an internal position. The internal olefins appear to form a

more lubricious layer at the metal surface and are recognized as better lubricants. Another significant application for C_{16}-C_{18} olefins is in paper sizing. LAOs are, once again, isomerized into linear internal olefins which are then reacted with maleic anhydride to make an alkyl succinic anhydride (ASA), a popular paper sizing chemical.

C_{20}-C_{30} LAOs production capacity is only 5-10% of the total production of a LAO plant. They are used in a number of reactive and non-reactive applications, including as feedstocks to make heavy linear alkyl benzene (LAB) and low molecular weight polymers which are used to enhance properties of waxes.

2.5 Literature reviews

In this thesis, the deoxygenation of palmitic acids will be studied. The active catalysts will require a considerable amount of oxygen vacancies on the surface. These oxygen vacancies, being very active, will interact with the carboxylic group of the palmitic acid, leaving carbon monoxide and water as byproducts together with alkenes as a desired product. So far, this reaction has received only little attention. It has been reported [15] that a high surface area increases the number of oxygen vacancies of CeO_2 in catalytic dry reforming reaction. In another work [12,13,14], it was pointed out that certain divalent or trivalent substituted such *as* Cu, Co, and Zr create oxygen vacancies in substituted $Ce_{1-x}M_xO_2$ solids. CeO_2 will be employed as a base catalyst in this research.

CHAPTER 3

EXPERIMENTAL DETAILS

3.1 Reagents

1. Cerium(III) chloride heptahydrate (Fluka), ≥98.5%
2. Zirconium(IV) oxynitrate monohydrate (Acros), ≥99.5%
3. Copper(II) nitrate trihydrate (QRec), ≥99.5%
4. Cobalt(II) nitrate hexahydrate (Carlo Erba), ≥99%
5. Cerium(IV) oxide (Aldrich chemistry), ≥99%
6. Palmitic acid (Fluka), ≥98%
7. *p*-xylene (Gehalf), >99%
8. Ammonia (Carlo Erba), 30% solution in water
9. Sodium carbonate (Carlo Erba), ≥99.7%
10. Cetyltrimethylammonium bromide, CTAB (Fluka), ≥98%
11. Acetone (Fisher Scientific), AR-grade
12. Hydrogen gas (Praxair), High purity
13. Air zero (Praxair), High purity
14. Nitrogen gas (Praxair), High purity

3.2 Equipment and tools

1. Catalyst testing rig
2. Tube furnace
3. Gas chromatograph (HP 6890 gas chromatography)
4. Vial
5. Stirrer
6. Dewar
7. Oven
8. Wash bottle
9. Laboratory glassware
10. Laboratory plasticware

11. X-ray Powder Diffractometer (Rigaku, DMAX 2200/Ultima+, Faculty of Science, Chulalongkorn University)

12. Gas adsorption analysis unit (Autosorb-1C, Quantachrome, Faculty of Science, KMITL)

13. Temperature programmed reduction (TPR) (Housemade)

14. Raman spectrometer (DXR Smart Raman, Thermoscientific, College of Nanotechnology, KMITL)

15. Scanning electron microscope (SEM) (EVO Ma10, Zeiss, College of Data Storage Innovation, KMITL)

3.3 Experimental procedure

3.3.1 Preparation of a catalyst

3.3.1.1 High surface area ceria

The high surface area CeO_2 was synthesized following the procedure in ref [15]. In a typical synthesis, 291 mL of an aqueous solution of 0.1 M CTAB was added dropwise into a beaker containing 364 mL of 0.1 M $CeCl_3 \cdot 7H_2O$. The molar ratio of cerium(III) cations to that of CTAB (Ce/CTAB) was kept constant at 0.8. The mixture was vigorously stirred, after which an aqueous ammonia solution was added dropwise into the mixture until pH value reached 11.5. The mixture was continuously stirred for another 3 h at room temperature, sealed and placed in a thermostatic bath maintained at 90°C for 3 days. After that, the mixture was cooled down to room temperature naturally. The resulting yellow precipitate was filtered and washed repeatedly with hot DI water (twice) and acetone (twice). It was dried overnight in an oven at 110°C, and then calcined in air at 450°C for 2.5 h.

3.3.1.2 Ceria-zirconia mixed oxide ($Ce_{0.8}Zr_{0.2}O_2$ and $Ce_{0.5}Zr_{0.5}O_2$)

The $Ce_{0.8}Zr_{0.2}O_2$ mixed oxide was synthesized by a co-precipitation method [12]. Two types of solution were prepared. The first one contained an equal volume of 0.1 M $ZrO(NO_3)_2 \cdot xH_2O$ and 0.1 M $CeCl_3 \cdot 7H_2O$, where the molar ratio of Zr to that of Ce is 1/4 corresponding to the stoichiometry $Ce_{0.8}Zr_{0.2}O_2$. Another type of the solution is aqueous ammonia. The solution of mixed metal cations was added dropwise into an aqueous solution of ammonia where the pH value was pre-adjusted to 9 with water. Additional volume of NH_3 was added to the mixture to maintain the pH value at 9 throughout the mixing. The purple precipitates were stirred

for 3 h at room temperature, filtered, washed with hot distilled water, dried at 110°C in air overnight, and then calcined in air at 450°C for 2.5 h. $Ce_{0.5}Zr_{0.5}O_2$ was prepared similarly employing the solution containing Zr^{4+} and Ce^{4+} at the molar ration 1/1.

3.3.1.3 Ceria-copper mixed oxide ($Ce_{0.8}Cu_{0.2}O_2$)

The $Ce_{0.8}Cu_{0.2}O_2$ mixed oxide was synthesized by the co-precipitation method [14] similar to that in Section 3.3.1.2. A well-mixed solution of $Cu(NO_3)_2 \cdot 3H_2O$ and $CeCl_3 \cdot 7H_2O$ (molar ratio Cu^{2+}/Ce^{4+} = 1/4) was prepared from the respective solution with a concentration of 0.1 M. This solution was added dropwise into a beaker containing a small amount of 1 M Na_2CO_3 where the pH value was pre-adjusted to 5.5 with water. Additional volume of 1 M Na_2CO_3 was added to the mixture if needed to maintain the pH value at 5.5 throughout the mixing. The blue precipitate was stirred for 3 h at room temperature. After that, it was filtered, thoroughly washed with hot distilled water, dried overnight at 110°C, and calcined in air at 450°C for 2.5 h.

3.3.1.4 Ceria-cobalt mixed oxide ($Ce_{0.8}Co_{0.2}O_2$)

The $Ce_{0.8}Co_{0.2}O_2$ mixed oxide [13] was also synthesized by a co-precipitation method. A well-mixed solution of $Co(NO_3)_2 \cdot 6H_2O$ and $CeCl_3 \cdot 7H_2O$ (molar ratio Co^{2+}/Ce^{4+} = 1/4) was prepared from the respective solution with a concentration of 0.1 M. This solution was added dropwise into a beaker containing a small amount of 1 M Na_2CO_3 where the pH value was pre-adjusted to 8.5. Additional volume of 1 M Na_2CO_3 is added to the mixture to keep the pH value constant at 8.5 throughout the mixing. The brown precipitate was aged at room temperature for 3 h at room temperature. The precipitate was then filtered and washed with hot distilled water several times, dried overnight at 110°C, and calcined in air at 450°C for 2.5 hr.

3.3.1.5 Commercial ceria

The commercial, low surface area ceria (LSA) catalyst was form Aldrich, 99%. It was calcined in air at 450°C for 2.5 h.

3.3.2 Characterization

3.3.2.1 X-ray powder diffraction (XRD)

The crystalline phase of the materials prepared can be identified, and the corresponding unit cell parameters can be determined, using XRD measurement. The sample was ground before it was packed on the sample holder. Analysis was done employing a Bruker diffractometer (Cu K_α radiation, 40 kV, 30 mA) at Department of Chemistry, Chulalongkorn University, covering the range 2θ = 5-90°, at the rate of 0.02°/step and a scanning rate of 0.4 s/step.

3.3.2.2 Determination of the surface area

Surface area of the materials can be determined by a Gas Adsorption Analyzer (Autosorb-1C, Quantachrome). Approximately, 0.02-0.04 g of the sample was loaded into the cell, which was subsequently heated to 350°C under vacuum so as to drive off the adsorbed gas from the surfaces. After that, nitrogen gas was introduced to the sample cell, and the N_2 adsorption at 77 K on the surfaces of the materials can be measured at the partial pressure (P/P_0) of 0.05-0.30. The adsorption isotherm was recorded and the corresponding surface area was analyzed using the method of Brunauer–Emmett–Teller (BET) [19].

3.3.2.3 Temperature-programmed reduction

Temperature-programmed reduction (TPR) provides information on how easy a species on the surfaces of a catalyst can be reduced. The sample weighed 50 mg was placed into a quartz tube reactor, which was located inside a temperature-regulated furnace. Prior to the measurement, each sample was heated to its calcination temperature (450°C in this work) in air zero and cooled to room temperature under N_2 gas. For TPR analysis, a 10% H_2 in Ar at the flow rate of 30 mL/min was applied, and the temperature was raised from 50°C up to 900°C at the heating rate of 5°C/min. Water molecules produced during the reduction was removed in a U-shape glass trap (cooled by the vapor of liquid N_2) before the carrier gas entering the thermal conductivity detector (TCD), enabling the analysis of the reducibility of a catalyst.

3.3.2.4 Raman spectroscopy

The powder of the sample to be investigated was manually pressed into a pellet. Raman spectra were collected using a DXR Smart Raman (Thermoscientific) at College of Nanotechnology, KMITL, from 50-4000 cm^{-1}. The laser employed has the wavelength of 532 nm, and the laser power was 5 mW. A total of 15 spectra were collected per one sample, with the exposure time of 2 s each.

3.3.2.5 Scanning electron microscopy

The catalyst surface morphology was determined by SEM technique. The sample was manually dispersed on an SEM stub and then coated with a gold thin film. After that, the sample was placed in a chamber which was evacuated from ambient pressure to below 10^{-4} Torr. Then, the sample holder was adjusted, tilted and moved in the X, Y and Z directions. As a consequence, sample surface was viewed from almost any perspective

3.3.3 Catalytic activity testing

The investigations on the catalytic activity of the materials were conducted in a continuous fixed bed reactor made of a glass tube (length, 50 cm; outside diameter, 8 mm; inner diameter, 6 mm) under atmospheric pressure, using N_2 as a carrier gas unless indicated otherwise. The catalysts were pressed into a pellet, crushed and sieved to the size of 0.3-0.5 mm, before being packed into a reactor. The catalytic testing rig is illustrated in Figure. 3.1. The reactor was positioned at the center of a vertical tube furnace. The gas flow rate was controlled by a mass flow controller and was checked by a bubble flow meter. Before activity testing, the catalysts were activated by heating at 2°C/min to 450°C for two hours under the stream of air zero (30 mL/min). Then, the catalysts were reduced for two hours under the stream of hydrogen gas (30 mL/min) at several reduction temperatures, so as to enable the investigation of the effect of the reduction temperature (400°C) on the catalytic activity. In some runs, reduction of a catalyst prior to the reaction was omitted, so us to test the effect of the presence of oxygen vacancy on catalytic activity. The reactor was thereafter cooled (or heated) to the reaction temperature (400°C) under N_2 gas (15 mL/min), following by additional purging (1 h) after the required reaction temperature had been reached. After that, the reactant (5% palmitic acid in *p*-xylene) was fed into the reactor by an HPLC pump at the rate of 1.5 mL/h. The reaction was operated for a total time on stream (TOS) of 280 min. The products were collected in a vial by a condenser for 40 minutes.

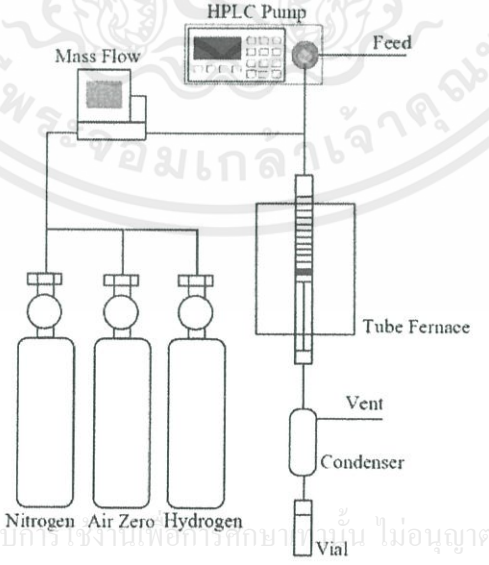

Figure 3.1 The catalytic test rig.

3.3.4 Product analysis

The reaction products from the catalytic testing in a continuous mode were analyzed with an HP 6890 gas chromatography equipped with a flame ionization detector (GC-FID) and a capillary column HP-5 (length, 30 m; internal diameter, 0.25 mm; film thickness, 0.025 μm). The following temperature program was used for the analysis of the collected liquid hydrocarbons: holding at 40°C for 10 min, followed by the ramping to 280°C at the rate of 15°C/min, before a final holding at that temperature for 60 min. N_2 gas was used as a carrier gas throughout.

CHAPTER 4

RESULT & DISCUSSIONS

4.1 X-ray diffraction

Unsubstituted high surface area (HSA) ceria, either in the as-synthesized form or after calcination, was yellow powder. The substitution of metal cations M (in parenthesis) to make $Ce_{1-x}M_xO_2$ resulted in a change in color from yellow to purple (Zr), green (Cu) and brown (Co) for the as-synthesized samples. After calcination at 450°C for 2.5 h, the catalyst doped with Zr changed to yellow, with Cu changed to brown, and with Co changed to olive-green.

Figure 4.1 depicts the XRD patterns of the prepared catalysts. All patterns can be indexed based on a cubic fluorite structure. The unit cell parameter *a* of the cubic cell for various catalysts are shown in **Table 4.1**, together with the crystallite size (calculated from the full width at half maximum (FWHM) of the 111 peaks) [13, 25-27]. Details can be found in **Appendix A**.

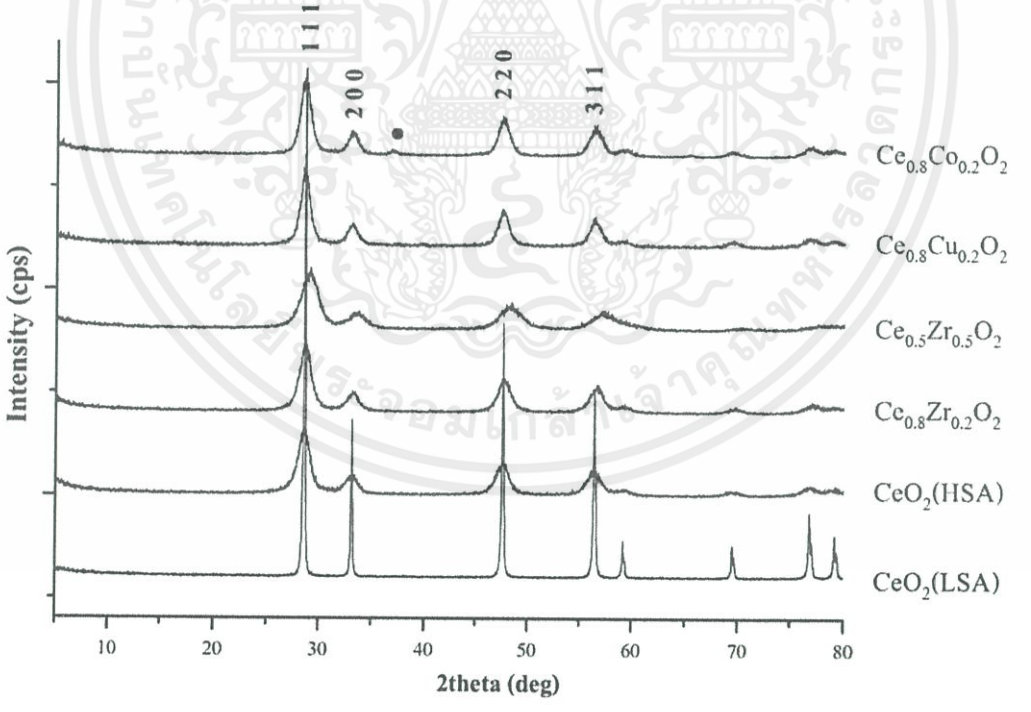

Figure 4.1 XRD patterns of ceria and metal-substituted ceria samples after calcination at 450°C for 2.5 h. The peak with • is the 311 reflection from Co_3O_4.

Table 4.1 Unit cell parameter, crystallite size and surface area of ceria and metal-substituted ceria. The standard deviation on the unit cell parameter in parenthesis belongs to the last digit.

Catalyst	FWHM (degree)	Unit cell parameter (Å)	Crystallite size (Å)	Surface area (m^2/g)
CeO_2 (LSA)	N/A	N/A	N/A	8
CeO_2 (HSA)	1.255	5.407(4)	65	159
$Ce_{0.8}Zr_{0.2}O_2$	1.140	5.39(1)	72	124
$Ce_{0.5}Zr_{0.5}O_2$	1.669	5.34(1)	49	93
$Ce_{0.8}Co_{0.2}O_2$	1.002	5.408(7)	82	42
$Ce_{0.8}Cu_{0.2}O_2$	0.976	5.42(1)	83	54

The reduction in unit cell parameter upon substituting Zr^{4+} with Ce^{4+} is expected and is in agreement with previous work [28-29] due to the smaller size of Zr^{4+} relative to Ce^{4+}. For an 8-fold coordination, the crystal radius for Zr^{4+} is 0.84 Å while that for Ce^{4+} is 0.97 Å [3]. The incorporation of large amount of Zr resulted in a large magnitude of unit cell parameter reduction as observed for $Ce_{0.5}Zr_{0.5}O_2$ (a = 5.34 Å) compared to $Ce_{0.8}Zr_{0.2}O_2$ (a = 5.39 Å).

The catalyst $Ce_{0.8}Co_{0.2}O_2$ has a slightly larger unit cell parameter than that of CeO_2. This is in contrary to the smaller size of Co^{2+} (0.90 Å for the coordination number of six). In this material, a deficiency in positive charge is created as a result of the replacement of Ce^{4+} by Co^{2+}. One way to bring back charge neutrality is by the reduction of Ce^{4+} into Ce^{3+} (1.143 Å for coordination number of eight), resulting in a larger unit cell for $Ce_{0.8}Co_{0.2}O_2$. An increase of unit cell parameter in cobalt-substituted ceria relative to the unsubstituted material has been reported previously [3]. In addition to a reduction of Ce^{4+} to Ce^{3+}, the creation of oxygen vacancy as a means to compensate for the deficiency in the positive charge cannot be discarded. However, the formation of Co_3O_4 could suggest that the incorporation of Co^{2+} into ceria is actually lower than the nominal formula of $Ce_{0.8}Co_{0.2}O_2$.

The expansion in the unit cell of $Ce_{0.8}Cu_{0.2}O_2$ as a result of doping by Cu^{2+} is in agreement with the previous work [30]. In this case, the rational based on crystal radii is even less straightforward. Ce^{4+} can have a coordination number up to 8, while the highest tabulated crystal radius of Cu^{2+} is 0.73 Å for a 6-fold coordination. Cu^{2+} is a d^9 cation, which could prefer the square planar arrangement instead of cubic (as in Ce^{4+}). Therefore, structural distortion in lattice

can be expected, producing oxygen vacancy, which in a theoretical study was found to increase the unit cell parameter [31].

4.2 Textural properties

The specific surfaces areas of ceria based catalysts as determined by N_2 adsorption/desorption are shown in **Table 4.1**. Details can be found in **Appendix B1-B12**. A high value of surface area obtained for HSA CeO_2 is as expected from the use of CTAB surfactant. The surface area of $Ce_{0.8}Cu_{0.2}O_2$ and $Ce_{0.8}Co_{0.2}O_2$ is not as high because these two catalysts were synthesized by a common co-precipitation method. Still, the surface areas obtained are close to the value reported despite of a slight difference in calcination temperature in our work and in [13-15]. A relatively high surface area of $Ce_{0.8}Zr_{0.2}O_2$ is also similar to the value reported in [12].

The morphology of catalysts were analyzed by Scanning Electron Microscope. The morphology of ceria (HSA) and commercial ceria (low surface area, LSA) used in this work can be seen in **Figure 4.2**.

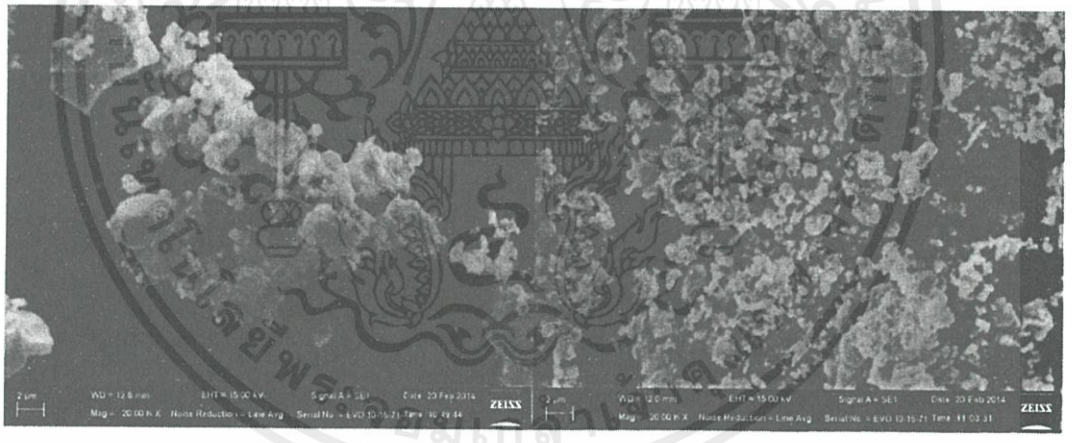

Figure 4.2 SEM of ceria (HSA) (left) and commercial ceria (LSA) (right).

It can be seen that, both ceria (HSA) and commercial ceria (LSA) showed non-uniform crystallites.

4.3 Temperature programed reduction

Temperature programmed reduction profiles of ceria based catalysts determined in the temperature range T = 50-900°C are shown in **Figure 4.3**. This technique determines the number

of reducible species based on the area under the peak, and determines their strength based on the temperature at the maximum peak intensity.

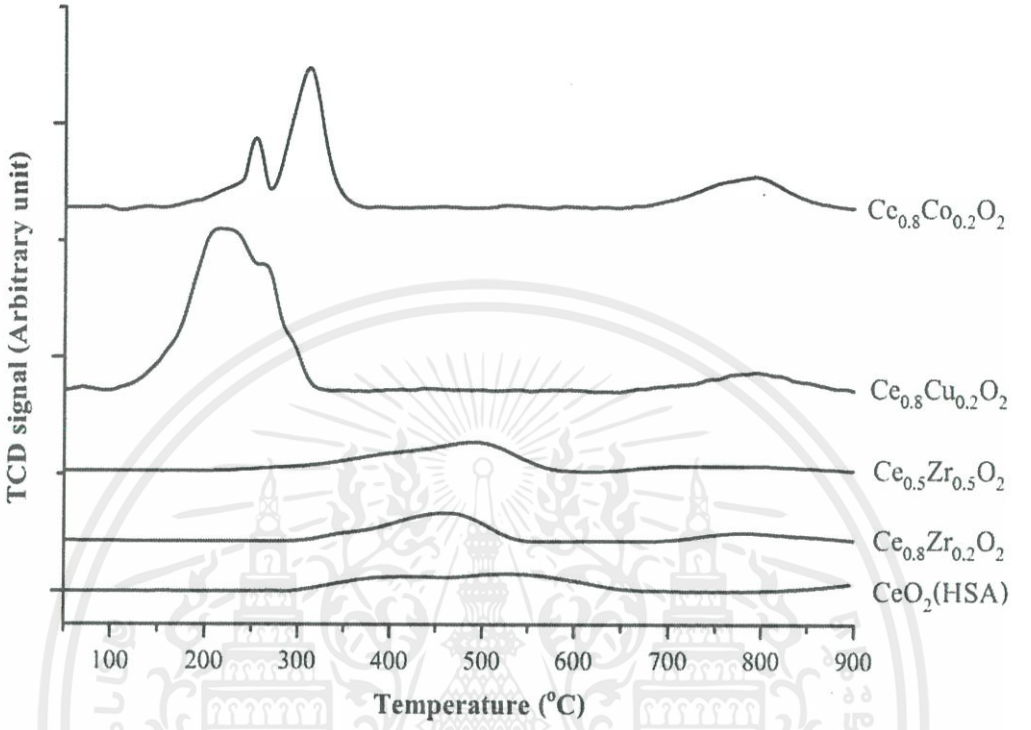

Figure 4.3 TPR profiles of ceria and metal-substituted ceria catalysts.

The TPR pattern of HSA ceria exhibits a broad band at 400-600°C and another one at around 800°C. The former can be ascribed to the reduction of oxygen vacancy on surface attached to surface Ce^{4+}, while the latter is referred to the reduction of bulk ceria [32]. Upon doping with Zr as in $Ce_{0.8}Zr_{0.2}O_2$, the catalyst became easily reduced as seen from the shift of both broad peaks to lower temperature compared to unsubstituted CeO_2. The smaller Zr^{4+} (compared to larger Ce^{4+}) prefers a 7-fold coordination number instead of the usual 8-fold coordination in fluorite structure [28]. The excess oxygen is therefore expelled from the crystal, resulting in an oxygen vacancy. Zr^{4+} in the mixed oxide is not easily reduced in the presence of Ce^{4+} [31]. The substitution with a larger amount of Zr^{4+} (as in $Ce_{0.5}Zr_{0.5}O_2$) results in the formation of oxygen vacancy which is more difficult to get reduced compared to $Ce_{0.8}Zr_{0.2}O_2$, as seen from the shift of peak temperature to a higher value. Yet, the amount of oxygen vacancy (i.e., peak area) is greater for $Ce_{0.5}Zr_{0.5}O_2$ than it is in $Ce_{0.8}Zr_{0.2}O_2$.

The $Ce_{0.8}Cu_{0.2}O_2$ catalyst exhibits two reduction peaks in the temperature range 100-300°C which corresponds to a stepwise reduction of $Cu^{2+} \rightarrow Cu^{+} \rightarrow Cu^{0}$ [32]. Yet, the presence of oxygen vacancy might be inferred from the increase in unit cell parameter as mentioned in **Section 4.1.**

The $Ce_{0.8}Co_{0.2}O_2$ had two reduction peaks in range of temperature 250-350°C, also corresponding to a step-wise process of $Co^{3+} \rightarrow Co^{2+} \rightarrow Co^{0}$ [13]. Since only Co^{2+} is present in $Ce_{0.8}Co_{0.2}O_2$, the reduction of $Co^{3+} \rightarrow Co^{2+}$ is derived from the presence of isolated Co_3O_4, as seen by XRD. Similar to copper-substituted ceria, the presence of oxygen vacancy in $Ce_{0.8}Co_{0.2}O_2$ might be deduced from the increase in unit cell parameter as discussed in **Section 4.1**. **Table 4.2** lists the peak positions of various catalysts studied.

Table 4.2 TPR peaks position of ceria and metal-substituted ceria catalysts.

Catalyst	T (°C)
CeO_2 (HSA)	403, 537, Higher than 800
$Ce_{0.8}Zr_{0.2}O_2$	422, 473, 792
$Ce_{0.5}Zr_{0.5}O_2$	433, 521, 822
$Ce_{0.8}Cu_{0.2}O_2$	215, 262, 785
$Ce_{0.8}Co_{0.2}O_2$	251, 310, 781

4.4 Raman spectroscopy

Raman spectra of the catalysts are shown in **Figure 4.4**. The spectra for all samples were dominated by a strong band at 460 cm^{-1} assigned to the F_{2g} Raman active mode of the fluorite CeO_2 [33]. In metal-substituted ceria after calcination, the F_{2g} peak shifted to a higher wavenumber (Zr, 463 cm^{-1}) but to lower wavenumber for Cu (446 cm^{-1}) and Co (449 cm^{-1}). A shift to higher wavenumber indicates a strengthening of the bond [28], in agreement with the reduction in unit cell parameter for Zr-substituted ceria compared to unsubstituted ceria in **Section 4.1**. By the same analogy, a shift to lower wavenumber indicates a weakening of the bond, also in agreement with the increase in unit cell parameter of Co- and Cu-substituted ceria. A larger shift to the lower-wavenumber in $Ce_{0.8}Cu_{0.2}O_2$ (446 cm^{-1}) is in agreement with its larger unit cell parameter (5.42 Å) compared to $Ce_{0.8}Co_{0.2}O_2$ (449 cm^{-1}, 5.408(3) Å).

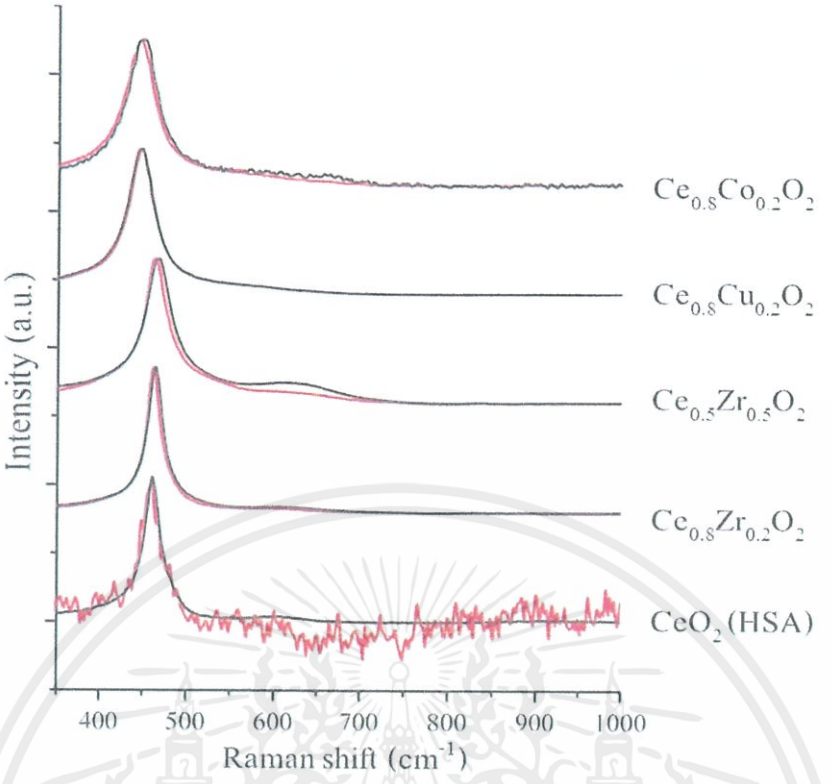

Figure 4.4 Raman spectra of ceria and metal-substituted ceria samples before (red) and after calcination (black) at 450°C for 2.5 h.

The peak at 600 cm^{-1} is generally ascribed to O^{2-} vacancy originated from non-stoichiometry in ceria [34]. The presence of this band in $Ce_{0.8}Zr_{0.2}O_2$ and $Ce_{0.5}Zr_{0.5}O_2$ is in good agreement with TPR profiles reported in **Section 4.1.3**. A stronger intensity of the 600 cm^{-1} band in $Ce_{0.5}Zr_{0.5}O_2$ suggests a larger concentration of oxygen vacancy relative to $Ce_{0.8}Zr_{0.2}O_2$, in agreement with TPR. Unsubstituted ceria did not show the presence of oxygen vacancy by Raman, likely reflecting the low amount of the vacancy. In addition to this reason, for $Ce_{0.8}M_{0.2}O_2$ (M = Cu, Co), the lack of the 600 cm^{-1} band could be due to the stronger absorption of light by the sample as suggested by their color. The position of the bands and the corresponding FWHMs are shown in **Table C1** in the Appendix.

4.5 Deoxygenation of palmitic acid over ceria catalyst

The deoxygenation of palmitic acid over ceria catalyst is studied using continuous fixed bed reactor under atmospheric pressure. The products distribution are shown in **Figure 4.5**.

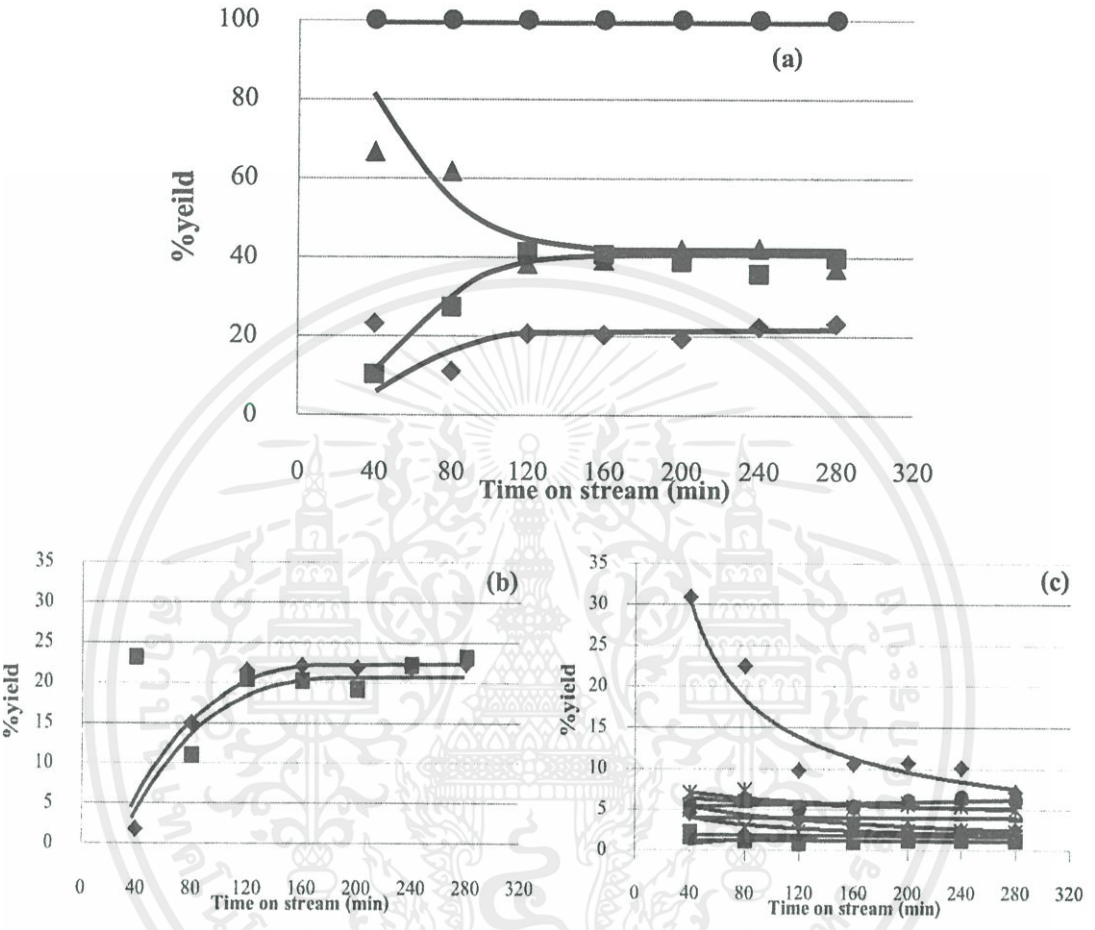

**Reaction condition; Catalyst: CeO_2 (HSA) Solvent: p-xylene, Reduction temperature: 400°C, Reaction temperature: 400°C, Flow rate of feed plus hydrogen carrier gas: 30 ml/min, Pressure: 1 atm, Contact time: 800 g.h/mol.*

Figure 4.5 (a) Conversion of palmitic acid (•) and yield (C_{31} ketone (♦), ketone/alcohol (■), hydrocarbons (▲))

(b) Yield of cracking ketone/alcohol products (C_{17} ketone (♦), heavy ketones/ alcohols (■))

(c) Yield of cracked hydrocarbon products. (light hydrocarbon(♦), C_9 (■), C_{10} (▲), C_{11} (X), C12 (*), C13 (•), C14 (+), C15 (-), C16 (–), C17 (♦))

It can be seen that a 100 % conversion is obtained, and major products are ketone/alcohol and hydrocarbons. It is interesting to note that yield of the ketone and the hydrocarbons are somewhat equivalent. In addition C31 ketone is observed as minor product.

It is suggested that C_{31} ketone is produced from ketonization of palmitic acid in a manner similar to typical reaction of carboxylic acid over ceria catalyst [35]. Two palmitic acid can adsorb on the ceria surface and coupling to a symmetry ketone (C_{31}ketone) bearing, carbon dioxide and water as shown in **Figure 4.6**.

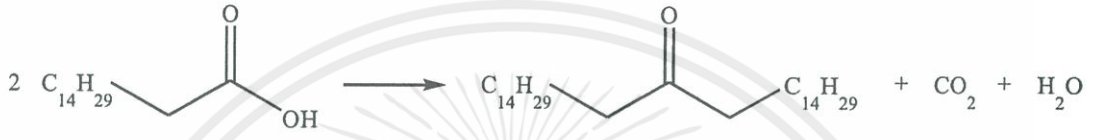

Figure 4.6 Ketonization of palmitic acid over ceria catalyst.

This can be confirmed by an observed carbon dioxide in exhausted gas from the reaction as shown in **Figure 4.7**. The gas products contain significant amount carbon dioxide and light hydrocarbons. Small amounts of carbon monoxide is also observed indicating that decarbonylation of palmitic acid also takes place.

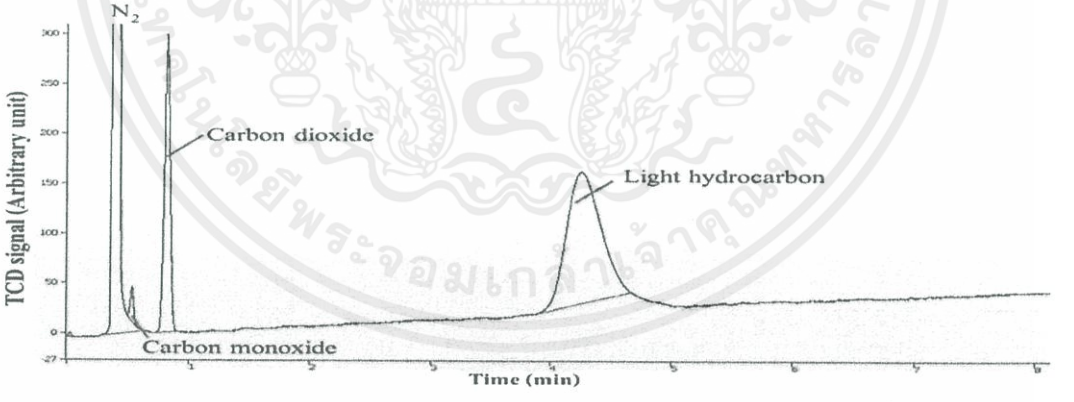

Figure 4.7 Chromatogram of gases product from palmitic acid over ceria catalyst.

As C_{17} ketone contains number of carbon higher than that of palmitic acid (C16 carboxylic acid), only explanation for C_{17} ketone is formation by cracking of C_{31} ketone. In line with this view, the mixtures of long chain hydrocarbon containing C_{14} or lower are obtained, together with C_{17} ketone, as demonstrated in **Figure 4.8.** Yield of this products are summarized in **Table 4.3**.

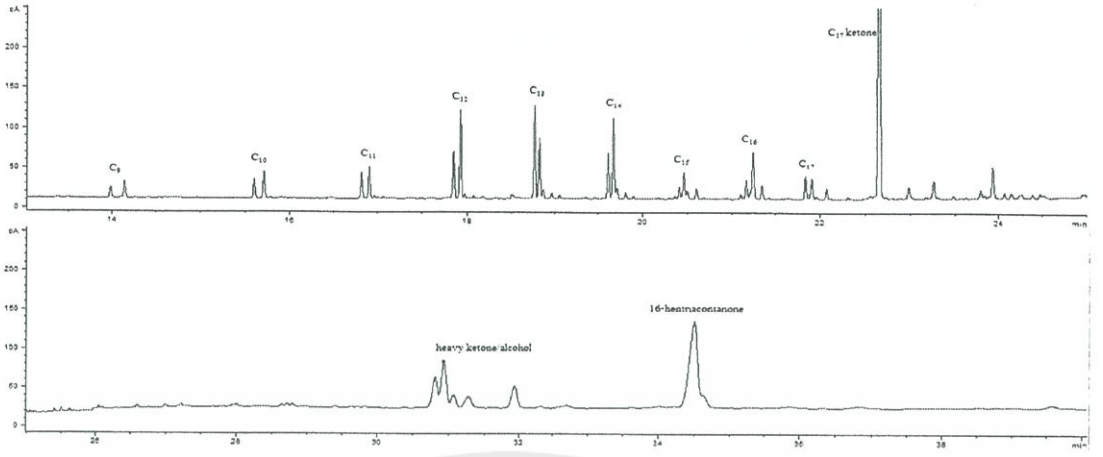

Figure 4.8 Chromatogram of hydrocarbon products from palmitic acid over ceria catalyst.

Table 4.3 Product distribution from palmitic acid over ceria catalyst.

%conversion	100
Product	% yield
16-hentriacontanone	21.6
heavy ketone/alcohol	16.2
2-heptadecanoe	21.9
Total hydrocarbon (unsat/sat)	40.3 (1.0)
C_{17}	2.5 (1.6)
C_{16}	3.9 (0.6)
C_{15}	2.3 (1.2)
C_{14}	5.4 (0.8)
C_{13}	6.2 (1.8)
C_{12}	5.4 (0.6)
C_{11}	2.3 (1.0)
C_{10}	1.8 (0.7)
C_9	1.3 (0.7)
light hydrocarbon	9.2

**Reaction condition; Catalyst: CeO_2 (HSA) Solvent: p-xylene, Reduction temperature: 450°C, Reaction temperature: 400°C, Flow rate of feed plus hydrogen carrier gas: 30 ml/min, Pressure: 1 atm, Contact time: 800 g.h/mol.*

Cracking of C_{31} ketone is likely to take place at the α-carbon of the carbonyl group because an intermediate (six membered ring) can be stabilized by intra-molecular hydrogen transfer to the carbonyl group as shown in **Figure 4.9**. Hence C_{17} ketone is predominantly produced while the remaining C_{14} long chain hydrocarbons can be cracked to other short chain counterparts. Accordingly yield of liquid hydrocarbon is lower than expected.

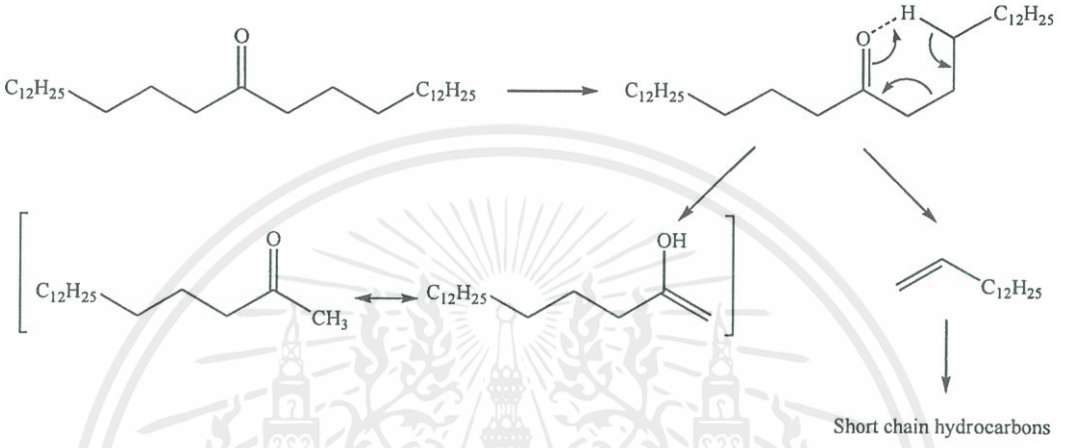

Figure 4.9 Main product of cracking of C_{31} ketone.

It is known that cracked product is generally unsaturation. The observed saturation of the cracked hydrocarbon products can be attributed to hydrogenation/hydrogen transfer of the hydrocarbon pools [36].

In addition to C_{17} ketone, heavy ketone/alcohol are obtained. It is suggested that, at high temperature, cracking of C_{31} ketone is not promoted only at the α-carbon, but also at any position along the alkyl chain of C_{31} ketone. In consistent with this, a noticeable yield of lower hydrocarbons is produced (Table 4.x1).

It is worth noting that significant yields of C_{16} and C_{17} long chain hydrocarbons are also observed. One cloud expects that, under hydrogen flow, competition adsorption of hydrogen on the oxygen vacancy can be facilitated. Accordingly, C_{16} long chain hydrocarbon could be obtained from reduction of palmitic acid to C_{16} aldehyde over the oxygen vacancy of the reduced ceria. This intermediate would be promptly hydrogenated to C_{16} alcohols that undergo hydrogenolysis to C_{16} saturated long chain hydrocarbon, as observed (**Figure 4.10**).

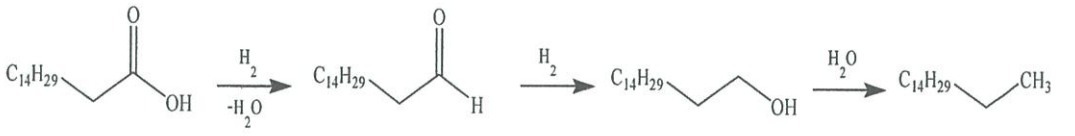

Figure 4.10 Production of C_{16} long chain hydrocarbon from palmitic acid.

In a similar manner, hydrogenation of C_{17} ketone to C_{17} alcohol is also possible. The C_{17} alcohol can be rapidly dehydrated to C_{17} long chain olefin as shown in **Figure 4.11**.

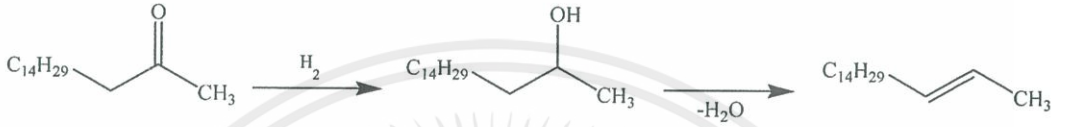

Figure 4.11 Production of C_{17} long chain hydrocarbon from C_{17} ketone.

In support with this view, C_{17} hydrocarbon is rich in unsaturated compounds while C_{16} hydrocarbon is predominantly saturation (**Table 4.3**). According to the above observation and discussion, the overall reaction pathway for deoxygenation of palmitic acid over ceria in hydrogen can be proposed in **Figure 4.12**.

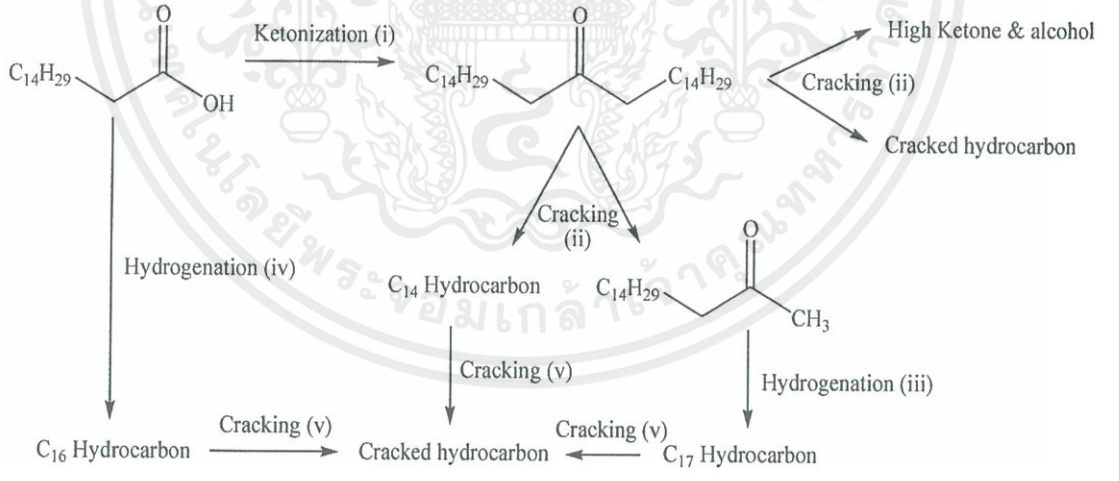

Figure 4.12 Pathway of palmitic acid over reduced ceria catalyst.

4.5.1 Role of oxygen vacancy

As the reaction of palmitic acid proceeds mainly via ketonization that promoted by oxygen vacancy of the ceria catalysts, the effect of oxygen vacancy in the catalyst can be demonstrated by the catalyst treatment as shown in the **Table 4.4**.

Table 4.4 Product distribution from palmitic acid in treated catalysts.

	reduced CeO_2 (HSA)	reduced CeO_2 (HSA)	non-reduced CeO_2 (HSA)
Carrier gas	in H_2	in N_2	in N_2
%Conversion	100	100	100
Product		% yield	
16-hentriacontanone	21.6	20.7	24.4
heavy ketone/alcohol	16.2	14.2	5.2
2-heptadecanoe	21.9	32.4	16.1
Total hydrocarbon (unsat/sat)	40.3 (1.0)	32.7 (0.9)	32.8 (1.4)
C_{17}	2.5 (1.6)	3.3 (1.2)	1.5 (2.4)
C_{16}	3.9 (0.6)	2.8 (0.5)	1.8 (3.0)
C_{15}	2.3 (1.2)	0.5 (1.4)	0.5 (4.7)
C_{14}	5.4 (0.8)	3.2 (0.7)	2.5 (2.4)
C_{13}	6.2 (1.8)	4.7 (1.9)	3.9 (3.1)
C_{12}	5.4 (0.6)	4.3 (0.5)	5.4 (0.6)
C_{11}	2.3 (1.0)	1.6 (1.2)	2.4 (1.1)
C_{10}	1.8 (0.7)	1.2 (0.9)	2.1 (0.8)
C_9	1.3 (0.7)	0.8 (0.9)	1.3 (0.7)
light hydrocarbon	9.2	10.3	11.4
Cracked acid	-	-	21.5
Coke[a]	2.6%	N/A	3.9%

**Reaction condition; Catalyst: CeO_2 (HSA) Solvent: p-xylene, Reduction temperature: 450°C, Reaction temperature: 400°C, Flow rate of feed plus carrier gas: 30 ml/min, Pressure: 1 atm, Contact time: 800 g.h/mol.*

[a] coke is detected by TGA (temperature about 800°C)

It can be seen that the reaction in hydrogen as carrier gas shows hydrocarbon yield higher than those from the reaction in the absence of hydrogen and from the non-reduced catalyst. This is because hydrogen gas can not only facilitate the formation of oxygen vacancy that promotes ketonization (i) but also promotes hydrogenation of palmitic acid (iv) and hydrogenation of C_{17} ketone (iii).

For the reaction in the absence of hydrogen as carrier gas, the reduced ceria is still active for ketonization (i) but hydrogenation (iii, iv) is limited. The only source of hydrogen is from the hydrogen transfer. Accordingly yields of C_{16} and C_{17} hydrocarbon are decreased. In line with this view, coke that is source of hydrogen transfer would be formed over the catalyst leading to faster deactivation as shown **in Figure 4.13.**

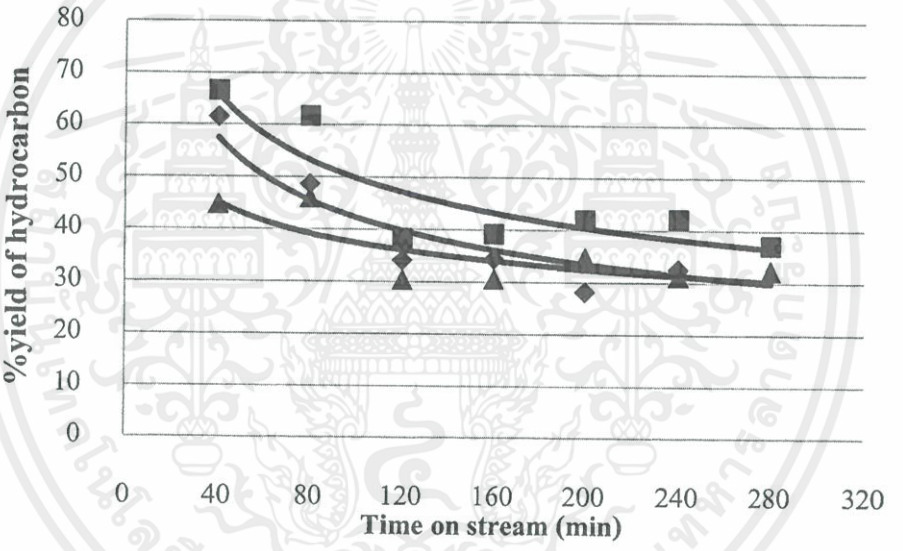

**Reaction condition; Catalyst: CeO_2 (HSA) Solvent: p-xylene, Reduction temperature: 450°C, Flow rate of feed plus carrier gas: 30 ml/min, Pressure: 1 atm, Contact time: 800 g.h/mol.*

Figure 4.13 Yield of hydrocarbon. (reduced ceria/H_2 (■), reduced ceria/N_2 (♦), non-reduced ceria/N_2 (▲))

This deactivation is clearly seen for the reaction with non-reduced catalyst. As the catalyst is not reduced, no oxygen vacancy is initially formed. However palmitic acid can decompose on ceria surface, generating oxygen vacancy that promoted ketonization and cracking to hydrocarbon in a manner similar to those primarily reduced. The decomposition of palmitic acid over this catalyst can be confirmed by the observed yield of cracked acid and coke as shown reaction in **Table 4.4.** TGA confirm that

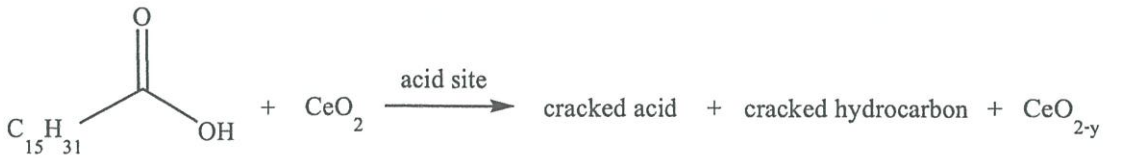

Figure 4.14 Reaction of palmitic acid to cracked acid.

In consistent with this view, faster deactivation is obtained and yield of hydrogenation product, C_{16} and C_{17} hydrocarbon are essentially low for the non-reduced catalyst (Table4.4). Furthermore, the cracked products are rich in unsaturated hydrocarbon.

According to the above observation and discussion, the overall reaction pathway for deoxygenation of palmitic acid over ceria catalyst can be amended by incorporating direct cracking of palmitic acid over non-reduced site, as shown in **Figure 4.15**.

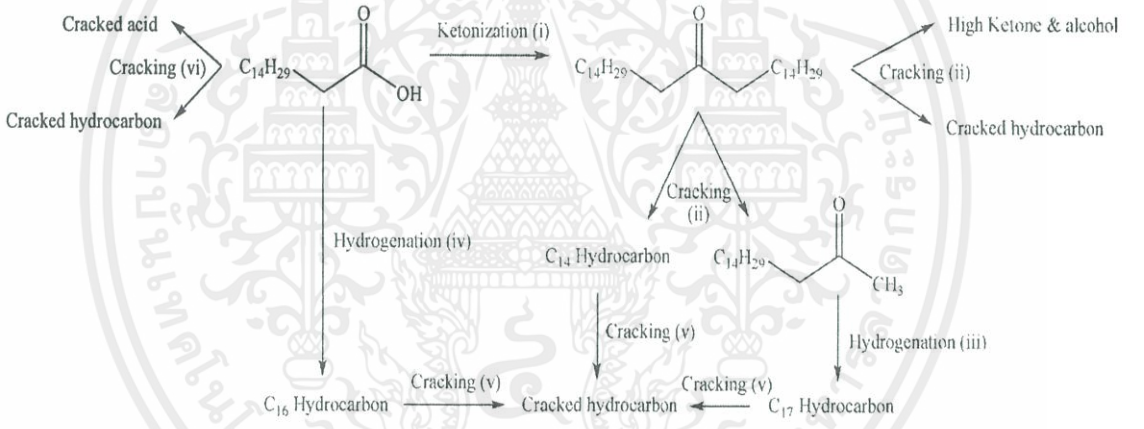

Figure 4.15 Overall pathway of palmitic acid over ceria catalyst.

4.5.2 Effect of particle size

As the formation of lattice oxygen mobility appears to strongly affect to the reaction of palmitic acid over the ceria catalyst, the effect of lattice oxygen mobility in CeO_2 (HSA) and Commercial CeO_2 (LSA) catalyst can be demonstrated in **Table 4.5**.

Table 4.5 Product distribution from palmitic acid over ceria (HSA) and ceria (Com.).

	CeO_2 (HSA)	CeO_2 (Com.)
%conversion	100	100
Product	% yield	
16-hentriacontanone	20.7	26.8
heavy ketone/alcohol	14.2	1.0
2-heptadecanoe	32.4	17.1
Total hydrocarbon (unsat/sat)	32.7 (0.9)	55.1 (0.0)
C_{17}	3.3 (1.2)	1.0 (0.0)
C_{16}	2.8 (0.5)	0.6 (0.0)
C_{15}	0.5 (1.4)	0.1 (0.0)
C_{14}	3.2 (0.7)	0.0 (0.0)
C_{13}	4.7 (1.9)	0.0 (0.0)
C_{12}	4.3 (0.5)	0.0 (0.0)
C_{11}	1.6 (1.2)	0.3 (-)
C_{10}	1.2 (0.9)	0.0 (0.0)
C_9	0.8 (0.9)	0.0 (0.0)
light hydrocarbon	10.3	53.1

**Reaction condition; Solvent: p-xylene, Reduction temperature: 450°C, Reaction temperature: 400°C, Flow rate of feed plus nitrogen carrier gas: 30 ml/min, Pressure: 1 atm, Contact time: 800 g.h/mol.*

It can be seen that yield of the hydrocarbon from the reaction over ceria (Com.) is higher than that using Ceria (HSA). This is because the particle size of ceria (Com.) is larger than that of ceria (HSA). As the oxygen vacancy is generated, the replenishment of the lattice oxygen from the bulk to the surface of CeO_2 (Com) is relatively slow, as compared to that in CeO_2 (HSA). Accordingly, the surface of CeO_2 (Com) remains defected, leading to the formation of Lewis acid site on the ceria surface. Hence cracking (v) of hydrocarbon is largely promoted over this catalyst, producing light hydrocarbons, as observed. In a support manner, yield of C_{17} ketone (2-heptadecanone) and heavy ketone/alcohol are exceedingly decreased.

4.5.3 Effect of incorporated metals

It is clear from the previous results that mobility of the lattice oxygen is essential for catalytic activity and selectivity. This can be modified by incorporation of other metal into CeO_2. The product distribution of Cu, Co, and Zr are compared in **Table 4.6.**

Table 4.6 Products distribution from palmitic acid over ceria (HSA) and difference metal incorporate ceria.

	CeO_2 (HSA)	$Ce_{0.8}Zr_{0.2}O_2$	$Ce_{0.8}Cu_{0.2}O_2$	$Ce_{0.8}Co_{0.2}O_2$
%conversion	100	100	100	100
Product		% yield		
16-hentriacontanone	20.7	11.1	27.6	18.9
heavy ketone/alcohol	14.2	4.8	5.6	1.8
2-heptadecanoe	32.4	50.9	2.5	28.6
Total hydrocarbons (unsat/sat)	32.7 (0.9)	33.2 (0.6)	64.3 (1.0)	50.7 (2.2)
C_{17}	3.3 (1.2)	4.4 (2.3)	1.6 (0.0)	0.5 (0.0)
C_{16}	2.8 (0.5)	5.8 (0.2)	0.0 (-)	0.0 (-)
C_{15}	0.5 (1.4)	0.7 (1.0)	0.0 (-)	0.0 (-)
C_{14}	3.2 (0.7)	4.7 (0.5)	1.3 (1.5)	8.6 (6.3)
C_{13}	4.7 (1.9)	2.9 (1.9)	1.2 (5.0)	4.7 (9.1)
C_{12}	4.3 (0.5)	5.0 (0.4)	0.7 (0.8)	3.1 (0.6)
C_{11}	1.6 (1.2)	1.4 (0.9)	0.6 (1.4)	2.1 (1.3)
C_{10}	1.2 (0.9)	1.5 (0.6)	1.1 (2.2)	2.9 (0.8)
C_9	0.8 (0.9)	0.4 (0.0)	0.2 (-)	2.3 (1.1)
light hydrocarbon	10.3	6.4	57.6	26.5

**Reaction condition; Solvent: p-xylene, Reduction temperature: 450°C, Reaction temperature: 400 °C, Flow rate of feed plus nitrogen carrier gas: 30 ml/min, Pressure: 1 atm, Contact time: 800 g.h/mol.*

It can be seen that yield of hydrocarbons from reaction over Cu and Co doped in catalyst is higher than that Zr doped over catalyst. However, light hydrocarbon is mainly produced. This is because Cu and Co in the solid solution are reduced to Cu^0 and Co^0 at 400°C as shown in TPR

(**Figure 4.3.**) Accordingly, number of surface defects is generated upon reduction of the catalyst. These defects act as strong acid sites promoting cracking of ketones and liquid hydrocarbons, to light hydrocarbon as discussed earlier. As seen for **Table 4.6**, only light hydrocarbon is obtained for $Ce_{0.8}Cu_{0.2}O_2$ while liquid hydrocarbons are retained for $Ce_{0.8}Co_{0.2}O_2$. This suggests that $Ce_{0.8}Cu_{0.2}O_2$ possess a higher cracking activity as compare to $Ce_{0.8}Co_{0.2}O_2$. In contrast, Zr is cannot be reduced and remain as a mixed oxide as seen from XRD. Moreover, Zr can improve lattice oxygen mobility [31] and hence facilitate the formation of oxygen vacancy. Therefore, $Ce_{0.8}Zr_{0.2}O_2$ can really promote ketonization (i). Accordingly, Zr is additional loaded in CeO_2 and the result is shown in **Table 4.7**.

Table 4.7 Products distribution from palmitic acid in p-xylene over Ceria-zirconia mixed oxide difference mole ratio.

	$Ce_{0.8}Zr_{0.2}O_2$	$Ce_{0.5}Zr_{0.5}O_2$
%conversion	100	100
Product	% yield	
16-hentriacontanone	11.1	16.3
heavy ketone & alcohol	4.8	5.1
2-heptadecanoe	50.9	47.5
Total hydrocarbons (unsat/sat)	33.2 (0.6)	31.1 (0.6)
C_{17}	4.4 (2.3)	1.4 (1.0)
C_{16}	5.8 (0.2)	6.2 (0.3)
C_{15}	0.7 (1.0)	0.5 (1.7)
C_{14}	4.7 (0.5)	4.0 (0.4)
C_{13}	2.9 (1.9)	4.6 (1.3)
C_{12}	5.0 (0.4)	4.3 (0.6)
C_{11}	1.4 (0.9)	1.4 (0.8)
C_{10}	1.5 (0.6)	1.4 (0.8)
C_9	0.4 (0.0)	0.8 (1.3)
light hydrocarbon	6.4	6.5

**Reaction condition; Solvent: p-xylene, Reduction temperature: 450°C, Reaction temperature: 400 °C, Flow rate of feed plus nitrogen carrier gas: 30 ml/min, Pressure: 1 atm, Contact time: 800 g.h/mol.*

It can be seen that product distribution from the deoxygenation of palmitic acid over $Ce_{0.8}Zr_{0.2}O_2$ and $Ce_{0.5}Zr_{0.5}O_2$ catalyst are similar. Hence, different Zr loading does not significantly effects the lattice oxygen mobility and hence, the deoxygenation of palmitic acid.

CHAPTER 5

CONCLUSION AND SUGGESTION

5.1 Conclusion

The XRD pattern of all catalysts showed a cubic fluorite structure of mixed metal oxides. The surface area of CeO_2 (HSA) obtained from precipitation with CTAB surfactants is relatively higher (159 m^2/g), as compared to that of other catalysts. TPR of $Ce_{0.5}Zr_{0.5}O_2$ showed relatively high H_2 consumption, as compared to CeO_2. While $Ce_{0.8}Cu_{0.2}O_2$ and $Ce_{0.8}Co_{0.2}O_2$ can be easily reduced, due to the presence of Cu and Co. Together with TPR results, Raman spectroscopy of $Ce_{0.5}Zr_{0.5}O_2$ indicates the presence of oxygen vacancy at 550-650 cm^{-1}.

From the deoxygenation of palmitic acid, it is found that C_{31} ketone is produced from ketonization of co-adsorption palmitic acids over the oxygen vacancy sites. This C_{31} ketone can be further cracked to C_{17} ketone, heavy ketone/alcohol and various types of unsaturated and saturated long chain hydrocarbons. The liquid hydrocarbon can also undergo cracking to short chain hydrocarbons over the Lewis acid site, generated along with the oxygen vacancy. The reaction over the reduced CeO_2 (HSA) catalyst under H_2 flow, does not only promote ketonization but also hydrogenation of palmitic acid and the C_{17} ketone produced. A direct hydrogenation of palmitic acid gives C_{16} saturated long chain hydrocarbon while hydrogenation of C_{17} ketone results in C_{17} unsaturated counterparts. The observed hydrogenation activity is due to a competitive adsorption of H_2 on the oxygen vacancy site, against co-adsorption of the two palmitic acids. For the reaction in an absence of hydrogen, the reduce ceria is still active for ketonization but hydrogenation is limited. This is because the only source of hydrogen is produced by hydrogen transfer from coke formation. In a different manner, palmitic acid can decompose on ceria surface to cracked acid in the reaction over non-reduced catalyst. However, the decomposition of palmitic acid leads to generation of additional oxygen vacancy/Lewis acid sites that promotes ketonization and cracking to lower hydrocarbons. The large particle size of CeO_2 inhibits the replenishment of the lattice oxygen from the bulk to the surface. Accordingly, Lewis acid site is largely generated over the catalyst with the large particle size (CeO_2 Com.) leading to cracking of liquid hydrocarbons to light hydrocarbons. Over $Ce_{0.8}Cu_{0.2}O_2$ and $Ce_{0.8}Co_{0.2}O_2$, Cu and Co are reduced bearing strong lewis acid site that again promotes cracking in

a manner similar to the catalyst with large particle size. It is noted that Cu possesses a higher cracking activity, as compared to Co. As $Ce_{0.8}Zr_{0.2}O_2$ possess large fraction of oxygen vacancy, ketonization and hydrogenation is highly promoted over this catalyst leading to high yield of C_{17} ketone and long chain hydrocarbons. Although oxygen vacancy in $Ce_{0.8}Zr_{0.2}O_2$ and $Ce_{0.5}Zr_{0.5}O_2$ are different, yield of the products obtained is somewhat similar. This is because the lattice oxygen mobility of these catalysts seem to be independent on the different Zr loading investigated.

5.2 Suggestion for Future Studies

5.2.1 It is interesting to vary contact time for study the reaction pathway for the deoxygenation of palmitic acid over cerium based catalyst.

5.2.2 In order to verify the competition between ketonization and hydrogenation over these catalysts, reactions with H_2 flow should be investigated.

5.2.3 Since C_{17} ketone is obtained as main products, it is interesting to incorporate a bifunctional catalyst to promote hydrogenation and dehydration of C_{17} ketone for the production of C_{17} long chain hydrocarbon.

REFERENCE

[1] C. Bianchini, G. Giambastiani, G. Mantovani, A. Meli. "Oligomerisation of ethylene to linear α-olfins by tetrahedral cobalt(II) precursors stabilised by benzo[b]thiophen-2-yl-substituted (imino)pyridine ligands" **Journal of Organometallic Chemistry**, vol. 689, 2004. pp. 1356–1361.

[2] A. Trovarelli. "Catalytic Properties of Ceria and CeO_2-Containing Materials" **Catalysis Reviews-science and Engineering**, vol. 38, 1996, 439-520.

[3] R. D. Shannon. "Revised effective ionic radii and systematic studies of interatomic distances in halides and chalcogenides" **Acta Crystallographica Section A**, vol. A32, 1976, pp. 751-767.

[4] R.J. Maria, F.M. Carmen, C. Abraham. "Influence of fatty acid composition of raw materials on biodiesel properties" **Bioresource Technology**, vol. 100, 2009. pp. 261-268.

[5] R. Alton, S .Cetinkaya, H.S. Yucesu. "The potential of using vegetable oil fule for diesel engine" **Energy Conversion and Management**, vol. 42, 2001. Pp. 529-538.

[6] Primary Information Services, "Fatty acid" [Online] http://www.primaryinfo.com/industry/fatty-acid.htm

[7] Wikipedia, "Deoxygenation" [Online] http://en.wikipedia.org/wiki/Deoxygenation

[8] A. Thursfield and I.S. Metcalfe, A. Kruth and J.T.S. Irvine. "Metal Oxides Chemistry and Applications"

[9] Wikipedia, "Cerium(IV) oxide" [Online] http://en.wikipedia.org/wiki/Cerium(IV)_oxide

[10] T. C. Charles, P.H.F. Charles. "oxygen vacancies and catalysis on ceria on ceria surface" **Science**, vol. 309, 2005. pp. 713-714.

[11] Jolla Kullgren. "Oxygen Vacancy Chemistry in Ceria" **Acta Universitatis Upsaliensis Uppsala**, 2012, pp. 9-14.

[12] N. Guillén-Hurtado, A. Bueno-López, A. García-García. "Effect of NO_x adsorption/ desorption over ceria-zirconia catalysts on the catalytic combustion of model soot" **Applied Catalysis B:Environment**, vol. 92, 2009, pp. 126-137.

[13] L.F. Liotta, G. Di Carlo, G. Pantaleo, A.M. Venezia, G. Deganello. "Co_3O_4/CeO_2 composite oxides for methane emissions abatement : Relationship between Co_3O_4–CeO_2 interaction and catalytic activity" **Applied Catalysis B:Environmental**, vol. 66, 2006, pp. 217–227.

[14] S. Hoˇcevar, U. Opara Krašovec, B. Orel, A. S. Aricó c, H. Kimd. "CWO of phenol on two differently prepared CuO–CeO_2 catalysts" **Applied Catalysis B:Environmental**, vol. 28, 2000, pp. 113–125.

[15] N. Laosiripojana , S. Assabumrungrat. "Catalytic dry reforming of methane over high surface area ceria" **Applied Catalysis B: Environmental**, vol. 60, 2005, pp. 107–116.

[16] Prof. Stephen A. Nelson, "X-Ray Crystallography" [Online] http://www.tulane.edu/~sanelson/eens211/x-ray.htm

[17] Yang Leng. "MATERIALS CHARACTERIZATION introduction to Microscopic and spectroscopic Methods" **John Wiley & Sons (Asia) Pte. Ltd.**, 2008, pp. 279-289.

[18] 2006 [Online] https://vscht.cz/kat/download/lab_tpr_eng.doc

[19] Björn Johannesson. "Verification of the BET-theory by Experimental Investigations on the Heat of Adsorption" **Lund Institute of Technology Division of Building Materials**, 2000, pp. 8-18.

[20] George Lappin (ed.) (1989). " Alpha Olefins Applications Handbook" [Online] http://en.wikipedia.org/wiki/Liner_alpha_olefin

[21] G.R. Lappin, L.H. Nemec, J.D. Sauer, J.D. Wagner. "Higher Olefins" **Kirk-Othmer Encyclopedia of Chemical Technology,** 2000, Vol. 17, pp. 709–728.

[22] P.W.N.M. Leeuwen, N.D. Clément, M.J.-L. Tschan. "New processes for the selective production of 1-octene" **Coordination Chemistry Reviews**, 2011, vol. 255, pp. 1499–1517.

[23] J. Skupinska. "Oligomerization of α-olefins to higher oligomers" **Chemical Review**, 1991, vol. 91, pp. 613–648.

[24] Y. Shiraki, Y. Nakamoto, Y. Souma "$ZrCl_4$-TEA-EASC three-component catalyst for the oligomerization of ethylene: the role of organoaluminum co-catalysts and additives" **Journal of Molecular Catalysis A: Chemical**, 2002, vol. 187, pp. 283–294.

[25] W. Yue, W. Zhou. "Porous crystals of cubic metal oxide templated by cage-containg mesoporous silica" **Journal of Materials Chemistry**, vol. 17, 2007, pp. 4947-4952

[26] A. Martı´nez-Arias, M. Ferna´ndez-Garcı´a, V. Ballesteros. "Characterization of High Surface Area Zr-Ce (1:1) Mixed Oxide Prepared by a Microemulsion Method" **Langmuir**, vol.15, 1999, pp. 4796-4802.

[27] D. Mrabet, A. Abassi, R. Cherizol. "One-pot solvothermal synthesis of mixed Cu-Ce-Ox nanocatalysts and their catalytic activity for low temperature CO oxidation" **Applied catalysis A : General**, vol. 447-448, 2012, pp. 60-66.

[28] M. Kuhn, S.R. Bishop, J.L.M. Rupp. "Structural characterization and oxygen nonstoichiometry of ceria-zirconia ($Ce_{1-x}Zr_xO_{2-\delta}$) solid solutions" **Acta Materialia**, vol. 61, 2013, pp. 4277–4288.

[29] J. A. Rodriguez, J. C. Hanson, J.-Y. Kim. "Properties of CeO_2 and $Ce_{1-x}Zr_xO_2$ Nanoparticles: X-ray Absorption Near-Edge Spectroscopy, Density Functional, and Time-Resolved X-ray Diffraction Studies" **Journal of Physical Chemistry B**, vol. 107, 2003, pp. 3535-3543.

[30] M. Narayanappa, V. D.B.C. Dasireddy, H. B. Friedrich. "Catalytic oxidation of n-octane over cobalt substituted ceria ($Ce_{0.90}Co_{0.10}O_{2-\delta}$) catalysts" **Applied Catalysis A : General**, vol. 447-448, pp. 135–143.

[31] X. Wang, J. A. Rodriguez, J. C. Hanson. "Unusual Physical and Chemical Properties of Cu in $Ce_{1-x}Cu_xO_2$ Oxides" **Journal of Physical Chemistry B**, vol. 109, 2005, pp. 19595–19603.

[32] A. Pintar, J. Batista, S. Hoˇcevar. "TPR, TPO, and TPD examinations of $Cu_{0.15}Ce_{0.85}O_{2-y}$ mixed oxides prepared by co-precipitation, by the sol–gel peroxide route, and by citric acid-assisted synthesis" **Journal of Colloid and Interface Science,** vol. 285, 2005, 218-231.

[33] J.C. Serrano-Ruiz, J. Luettich, A. Sepúlveda-Escribano. "Effect of the support composition on the vapor-phase hydrogenation of crotonaldehyde over $Pt/Ce_xZr_{1-x}O_2$ catalysts" **Journal of Catalysis**, vol. 241, 2006, pp. 45-55.

[34] Z.V. Popovic, Z.D. Mitrovic, M.J. Konstantinovic. "Raman scattering characterization of nanopowders and nanowires (rods)"**Journal of Raman Spectroscopy**, vol. 38, 2007, pp. 750-755.

[35] O. Nagashima, S. Sato, R. Takahashi. "Ketonization of carboxylic acids over CeO_2-based composite oxides" **Journal of Molecular Catalysis A: Chemical**, vol. 227, 2005, pp. 231-239.

[36] S. Wang, X. Li, F. Zhang. "Bio-oil catalytic reforming without steam addition: Application to hydrogen production and studies on its mechanism" **International Journal of Hydrogen Energy**, vol. 38, 2013, pp. 16038–16047.

Appendix A

X-ray powder diffraction

Table A1. List of peak positions (in 2θ), the corresponding values of d spacing, unit cell parameter a of the cubic cell, and hkl index for calcined (450°C 2.5 h) ceria based catalysts. The a values are (in the unit of Å): 5.4067±0.0037 (CeO_2 HSA), 5.3913±0.0102 ($Ce_{0.8}Zr_{0.2}O_2$), 5.3397±0.0132 ($Ce_{0.5}Zr_{0.5}O_2$), 5.4174±0.0132 ($Ce_{0.8}Cu_{0.2}O_2$), and 5.4075±0.0067 ($Ce_{0.8}Co_{0.2}O_2$).

			CeO_2(HSA)				$Ce_{0.8}Zr_{0.2}O_2$				$Ce_{0.5}Zr_{0.5}O_2$				$Ce_{0.8}Cu_{0.2}O_2$				$Ce_{0.8}Co_{0.2}O_2$			
h	k	l	2θ	θ	d(Å)	a(Å)	2θ	θ	d(Å)	a(Å)	2θ	θ	d(Å)	a(Å)	2θ	θ	d(Å)	a(Å)	2θ	θ	d(Å)	a(Å)
1	1	1	28.56	14.28	3.1228	5.4089	28.72	14.36	3.1058	5.3794	28.90	14.45	3.0868	5.3464	28.40	14.20	3.1401	5.4387	28.60	14.30	3.1184	5.4013
2	0	0	33.12	16.56	2.7026	5.4051	33.14	16.57	2.7010	5.4021	33.44	16.72	2.6775	5.3550	33.02	16.51	2.7105	5.4210	33.04	16.52	2.7089	5.4178
2	2	0	47.48	23.74	1.9133	5.4117	47.60	23.80	1.9087	5.3987	48.28	24.14	1.8835	5.3273	47.54	23.77	1.9111	5.4054	47.42	23.71	1.9156	5.4182
3	1	1	56.36	28.18	1.6311	5.4097	56.68	28.34	1.6227	5.3818	57.28	28.64	1.6071	5.3302	56.36	28.18	1.6311	5.4097	56.38	28.19	1.6306	5.4080
2	2	2	59.22	29.61	1.5589	5.4002	-	-	-	-	Average			5.3397	-	-	-	-	59.18	29.59	1.5600	5.4041
4	0	0	-	-	-	-	-	-	-	-	Standard deviation			0.0132	-	-	-	-	69.60	34.80	1.3498	5.3991
3	3	1	76.82	38.41	1.2398	5.4042	76.98	38.49	1.2376	5.3946					76.69	38.34	1.2417	54122	76.82	38.41	1.2398	5.4042
4	2	0	79.18	39.59	1.2087	5.4053	Average			5.3913					Average			5.4174	79.16	39.58	1.2089	5.4065
4	2	2	88.48	44.24	1.1041	5.4088	Standard deviation			0.0102					Standard deviation			0.0132	88.50	44.25	1.1039	5.4081
			Average			5.4067													Average			5.4075
			Standard deviation			0.0037													Standard deviation			0.0067

APPENDIX B

Gas adsorption analysis

Quantachrome Corporation
Quantachrome Autosorb Automated Gas Sorption System Report
Autosorb for Windows® Version 1.19

Sample ID	CeO2 cal 450 2 hr				
Description	BET 11 pts				
Comments					
Sample Weight	0.1085 g				
Adsorbate	NITROGEN	Outgas Temp	350.0 °C	Operator	BomB
Cross-Sec Area	16.2 Å²/molecule	Outgas Time	15.1 hrs	Analysis Time	137.3 min
NonIdeality	6.580E-05	P/Po Toler	2	End of Run	09/16/2013 1
Molecular Wt	28.0134 g/mol	Equil Time	3	File Name	560916_1.RAW
Station #	1	Bath Temp.	77.35		

Isotherm

P/Po	Volume [cc/g] STP
5.6020e-02	31.3281
7.6074e-02	33.1994
1.0049e-01	35.1945
1.2602e-01	37.1088
1.5112e-01	38.9688
1.7611e-01	40.7767
2.0094e-01	42.6047
2.2565e-01	44.4913
2.5038e-01	46.4168
2.7485e-01	48.4552
2.9890e-01	50.6981

Figure B1. Data on the isotherm of ceria (HSA) calcined at 450°C 2.5h

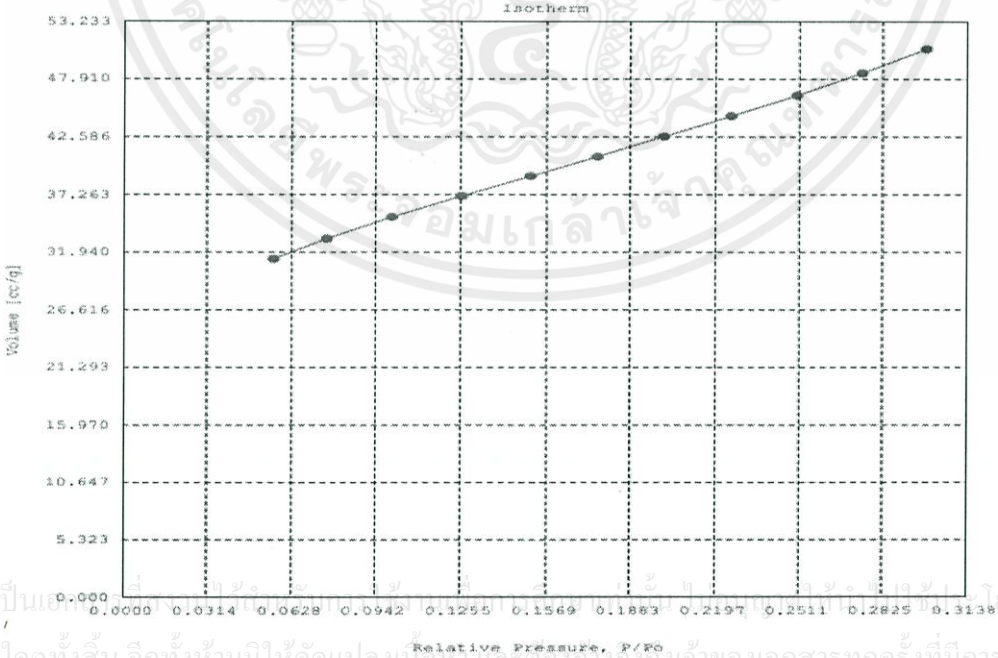

Figure B2. Isotherm of ceria (HSA) calcined at 450°C 2.5h

Sample ID	CeO2 LSA				
Description	Ads 22 Pts Des 22 Pts BET 11 pts				
Comments					
Sample Weight	0.0732 g				
Adsorbate	NITROGEN	Outgas Temp	300.0 °C	Operator	Best
Cross-Sec Area	16.2 Å²/molecule	Outgas Time	6.6 hrs	Analysis Time	268.3 min
NonIdeality	6.580E-05	P/Po Toler	2	End of Run	02/19/2014 0
Molecular Wt	28.0134 g/mol	Equil Time	2	File Name	570218_3.RAW
Station #	1	Bath Temp.	77.35		

Isotherm		Isotherm		Isotherm	
P/Po	Volume [cc/g] STP	P/Po	Volume [cc/g] STP	P/Po	Volume [cc/g] STP
5.5792e-02	1.1423	6.0685e-01	3.8177	5.9520e-01	6.7307
8.3593e-02	1.3596	6.5551e-01	4.5033	5.4676e-01	6.0896
1.0844e-01	1.6239	7.0463e-01	5.4109	4.9811e-01	5.7161
1.3330e-01	1.8504	7.5679e-01	6.1291	4.4868e-01	5.4014
1.5890e-01	1.9365	8.0443e-01	7.0369	3.9978e-01	4.8723
1.8340e-01	2.1432	8.5577e-01	8.2024	3.5090e-01	4.4703
2.0939e-01	2.0693	9.0470e-01	9.4379	3.0198e-01	3.9046
2.3342e-01	2.2506	9.5081e-01	11.8300	2.5228e-01	3.4691
2.5895e-01	2.3088	9.9689e-01	21.8243	1.9050e-01	2.7968
2.8417e-01	2.2288	9.4548e-01	13.0986	1.4271e-01	2.2179
3.0871e-01	2.2804	8.9280e-01	10.4982	9.3729e-02	1.7374
3.5861e-01	2.4257	8.4601e-01	9.4596		
4.0843e-01	2.5448	7.9858e-01	8.6998		
4.5737e-01	2.9785	7.4118e-01	7.6888		
5.0948e-01	3.0058	6.9294e-01	7.2715		
5.5808e-01	3.2558	6.4476e-01	6.8247		

Figure B3. Data on the isotherm of commercial ceria (low surface area, LSA) calcined at 450°C 2.5h

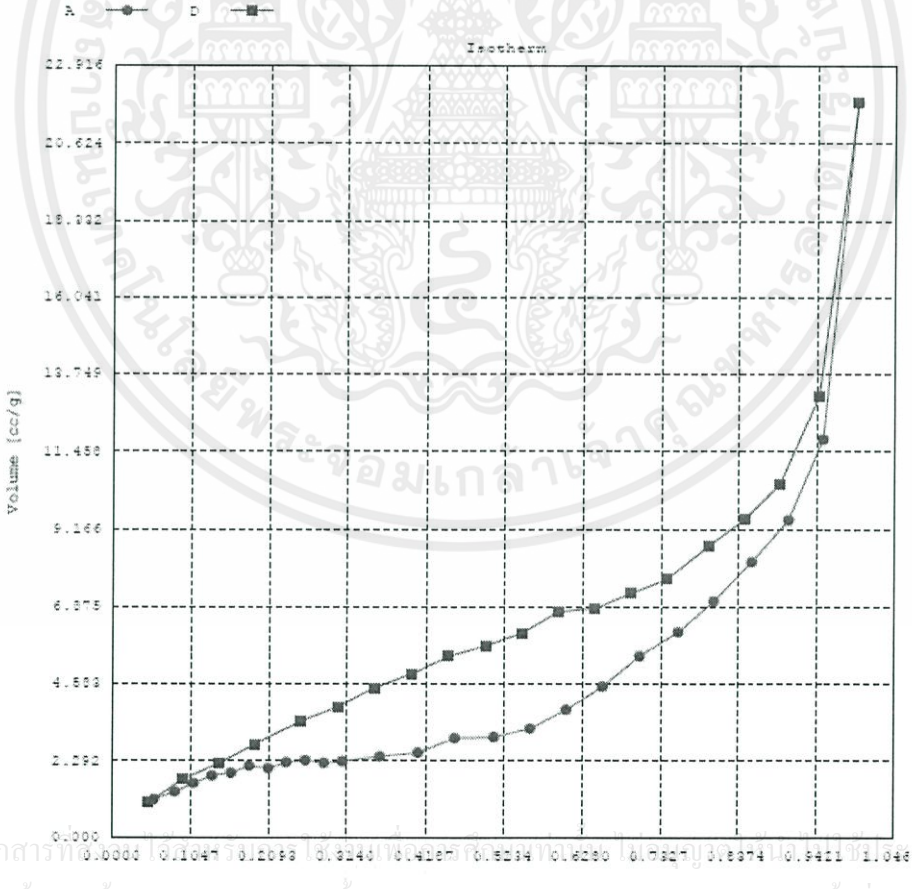

Figure B4. Isotherm of commercial ceria (low surface area, LSA) calcined at 450°C 2.5h

Quantachrome Corporation
Quantachrome Autosorb Automated Gas Sorption System Report
Autosorb for Windows® Version 1.19

Sample ID	Ce 0.8 Zr 0.2 O2 450C 2.5 hr.				
Description	Ads 22 Pts Des 22 Pts BET 11 pts				
Comments					
Sample Weight	0.1224 g				
Adsorbate	NITROGEN	Outgas Temp	300.0 °C	Operator	Best
Cross-Sec Area	16.2 Å²/molecule	Outgas Time	6.8 hrs	Analysis Time	370.1 min
NonIdeality	6.580E-05	P/Po Toler	2	End of Run	01/17/2014 2
Molecular Wt	28.0134 g/mol	Equil Time	2	File Name	170117_2.RAW
Station #	1	Bath Temp.	77.35		

Isotherm		Isotherm		Isotherm	
P/Po	Volume [cc/g] STP	P/Po	Volume [cc/g] STP	P/Po	Volume [cc/g] STP
5.6712e-02	24.2136	5.0148e-01	54.4374	7.8991e-01	90.0221
7.8262e-02	25.5977	5.5003e-01	58.0191	7.4864e-01	89.0613
1.0306e-01	27.0737	5.9918e-01	64.2154	6.9335e-01	88.3987
1.2775e-01	28.5532	6.4841e-01	69.7286	6.4111e-01	87.4575
1.5314e-01	30.0179	7.0274e-01	75.8516	5.9193e-01	85.9387
1.7990e-01	31.4876	7.5073e-01	80.9337	5.5073e-01	81.9771
2.0210e-01	33.0319	8.0227e-01	85.3897	5.0094e-01	68.7667
2.2777e-01	34.4747	8.5688e-01	88.5278	4.5068e-01	55.4721
2.5176e-01	36.1708	8.9305e-01	90.4150	3.9801e-01	49.4721
2.7611e-01	37.9129	9.4829e-01	92.4248	3.4860e-01	45.7032
3.0310e-01	39.3511	9.9297e-01	94.7075	2.9827e-01	41.9487
3.5459e-01	42.9829	9.4524e-01	92.6471		
4.0449e-01	46.6400	8.9297e-01	91.5253		
4.5303e-01	50.3732	8.5123e-01	90.8276		

Figure B5. Data on the isotherm of $Ce_{0.8}Zr_{0.2}O_2$ calcined at 450°C 2.5h

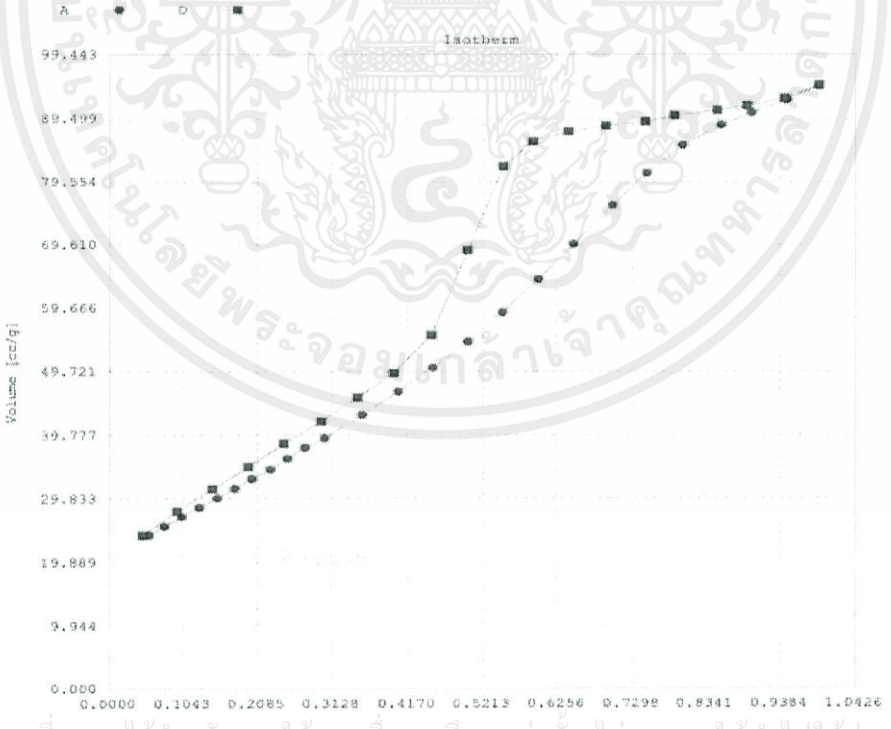

Figure B6. Isotherm of $Ce_{0.8}Zr_{0.2}O_2$ calcined at 450°C 2.5h

Quantachrome Corporation
Quantachrome Autosorb Automated Gas Sorption System Report
Autosorb for Windows® Version 1.19

Sample ID	Ce0.5 Zr0.5 O2				
Description	Ads 22 Pts Des 22 Pts BET 11 pts				
Comments					
Sample Weight	0.0904 g				
Adsorbate	NITROGEN	Outgas Temp	300.0 °C	Operator	BomB
Cross-Sec Area	16.2 Å²/molecule	Outgas Time	5.1 hrs	Analysis Time	316.5 min
NonIdeality	6.580E-05	P/Po Toler	2	End of Run	02/18/2014 1
Molecular Wt	28.0134 g/mol	Equil Time	2	File Name	570218_2.RAW
Station #	1	Bath Temp.	77.35		

Isotherm		Isotherm		Isotherm	
P/Po	Volume [cc/g] STP	P/Po	Volume [cc/g] STP	P/Po	Volume [cc/g] STP
5.4042e-02	17.6064	5.5405e-01	44.2337	6.9298e-01	54.2009
7.9036e-02	19.0700	5.9770e-01	47.0868	6.4328e-01	53.5937
1.0426e-01	20.5000	6.5526e-01	49.9416	5.9469e-01	53.1897
1.2948e-01	21.7848	7.0208e-01	51.9117	5.4611e-01	52.4499
1.5538e-01	22.9142	7.5266e-01	53.2382	4.9770e-01	51.7786
1.8028e-01	23.9580	8.0667e-01	54.1845	4.5287e-01	44.8948
2.0539e-01	24.9825	8.5529e-01	55.2225	4.0025e-01	37.0383
2.2995e-01	26.0997	9.0381e-01	56.4052	3.4607e-01	33.6252
2.5538e-01	27.0884	9.5460e-01	57.2966	2.9377e-01	30.8986
2.7963e-01	28.3053	9.9268e-01	59.9850	2.5032e-01	28.5956
3.0480e-01	29.4756	9.4431e-01	57.3265	1.9421e-01	25.7192
3.5075e-01	31.5261	8.9859e-01	56.3185	1.5049e-01	23.4397
3.9926e-01	34.2310	8.4835e-01	55.6937	9.4326e-02	20.2784
4.5509e-01	37.5585	8.0086e-01	55.1164		
4.9726e-01	40.4626	7.4111e-01	54.6723		

Figure B7. Data on the isotherm of of $Ce_{0.5}Zr_{0.5}O_2$ calcined at 450°C 2.5h

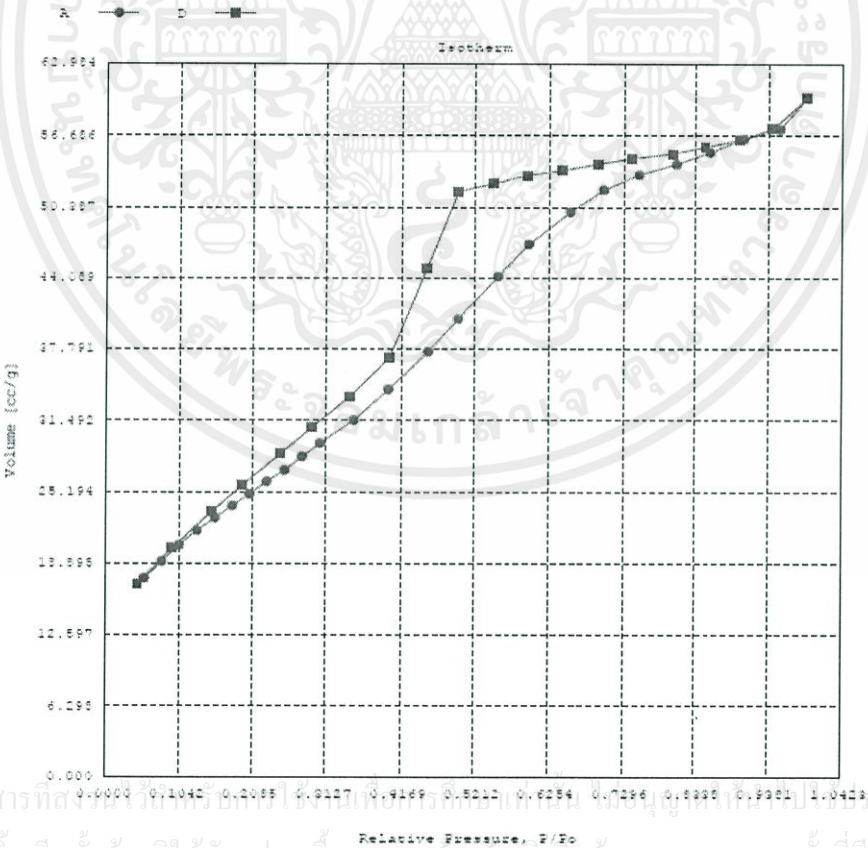

Figure B8. Isotherm of $Ce_{0.5}Zr_{0.5}O_2$ calcined at 450°C 2.5h

Quantachrome Corporation
Quantachrome Autosorb Automated Gas Sorption System Report
Autosorb for Windows® Version 1.19

Sample ID	Ce0.8Cu0.202 450oC				
Description	Ads 22 Pts Des 22 Pts BET 11 pts				
Comments					
Sample Weight	0.1054 g				
Adsorbate	NITROGEN	Outgas Temp	300.0 °C	Operator	Bom
Cross-Sec Area	16.2 Å²/molecule	Outgas Time	17.7 hrs	Analysis Time	471.0 min
NonIdeality	6.580E-05	P/Po Toler	2	End of Run	12/24/2013 1
Molecular Wt	28.0134 g/mol	Equil Time	2	File Name	561224_1.RAW
Station #	1	Bath Temp.	77.35		

Isotherm

P/Po	Volume [cc/g] STP
5.0325e-02	10.5073
8.0244e-02	11.6056
1.0671e-01	12.3230
1.3223e-01	12.9020
1.5694e-01	13.5131
1.8208e-01	14.1437
2.0727e-01	14.6974
2.3172e-01	15.3522
2.5732e-01	15.8766
2.8121e-01	16.7787
3.0654e-01	17.5161
3.5305e-01	19.2001
4.0261e-01	20.9737

Isotherm

P/Po	Volume [cc/g] STP
4.5129e-01	22.9385
5.0294e-01	24.7655
5.5059e-01	27.0878
5.9846e-01	29.8922
6.5450e-01	33.5173
7.0557e-01	37.0945
7.5323e-01	41.2502
8.0315e-01	45.3009
8.4846e-01	51.2223
9.0397e-01	61.4937
9.4775e-01	82.3925
9.9229e-01	190.5911

Figure B9. Data on the isotherm of $Ce_{0.8}Cu_{0.2}O_2$ calcined at 450°C 2.5h

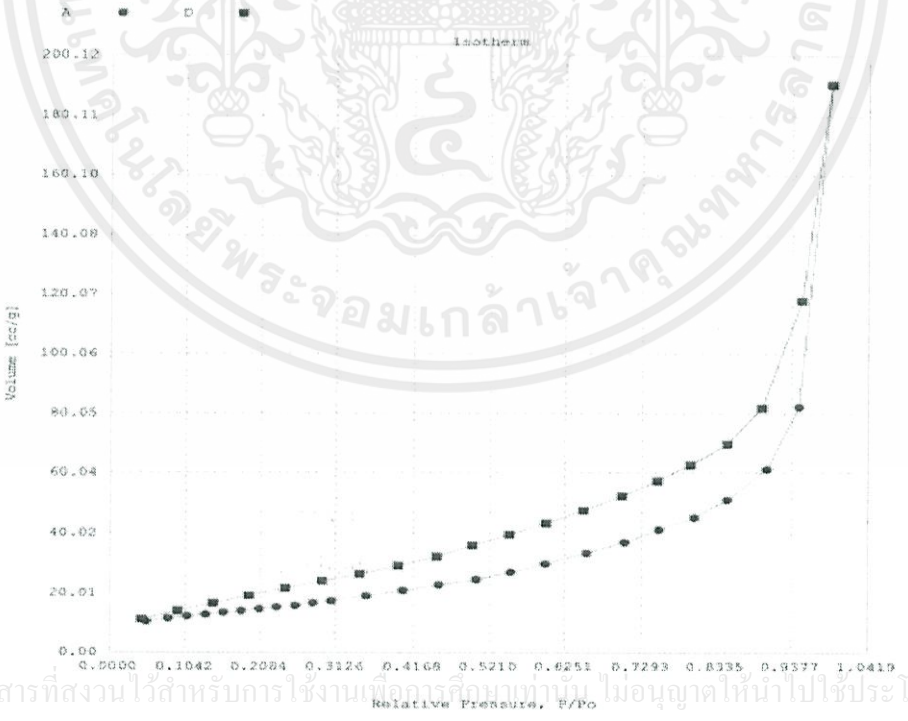

Figure B10. Isotherm of $Ce_{0.8}Cu_{0.2}O_2$ calcined at 450°C 2.5h

Quantachrome Corporation
Quantachrome Autosorb Automated Gas Sorption System Report
Autosorb for Windows® Version 1.19

Sample ID	CeCoO2 450C 2.5 hr				
Description	Ads 22 Pts Des 22 Pts BET 11 pts				
Comments					
Sample Weight	0.0537 g				
Adsorbate	NITROGEN	Outgas Temp	300.0 °C	Operator	Boom
Cross-Sec Area	16.2 Å²/molecule	Outgas Time	15.3 hrs	Analysis Time	354.9 min
NonIdeality	6.580E-05	P/Po Toler	2	End of Run	11/27/2013 1
Molecular Wt	28.0134 g/mol	Equil Time	2	File Name	561127_1.RAW
Station #	1	Bath Temp.	77.35		

Isotherm		Isotherm		Isotherm	
P/Po	Volume [cc/g] STP	P/Po	Volume [cc/g] STP	P/Po	Volume [cc/g] STP
5.7788e-02	8.6605	5.0577e-01	17.7440	7.9760e-01	42.4814
8.2872e-02	9.2212	5.5612e-01	18.0294	7.4695e-01	36.6147
1.0814e-01	9.6707	6.0595e-01	20.2177	6.9426e-01	32.3266
1.3339e-01	10.0653	6.5336e-01	22.7456	6.4980e-01	29.0952
1.5783e-01	10.3963	7.0260e-01	25.2920	5.9275e-01	26.4235
1.8348e-01	10.9025	7.5075e-01	28.4026	5.4568e-01	24.7274
2.0748e-01	11.5769	7.9753e-01	32.7149	4.9860e-01	22.9601
2.3334e-01	12.0032	8.5006e-01	40.8648	4.5019e-01	21.2115
2.5798e-01	12.5258	9.0277e-01	53.2827	3.9149e-01	19.3616
2.8311e-01	12.9513	9.4793e-01	68.0480	3.4474e-01	17.7680
3.0792e-01	13.4766	9.9227e-01	119.0352	2.9611e-01	16.3135
3.5706e-01	14.2785	9.4931e-01	76.8572	2.4727e-01	14.9121
4.0661e-01	15.3111	8.9589e-01	60.4596	1.9840e-01	13.3908
4.5660e-01	16.6444	8.5060e-01	53.0711	1.4981e-01	11.9567
				1.0074e-01	10.5615

Figure B11. Data on the isotherm of $Ce_{0.8}Co_{0.2}O_2$ calcined at 450°C 2.5h

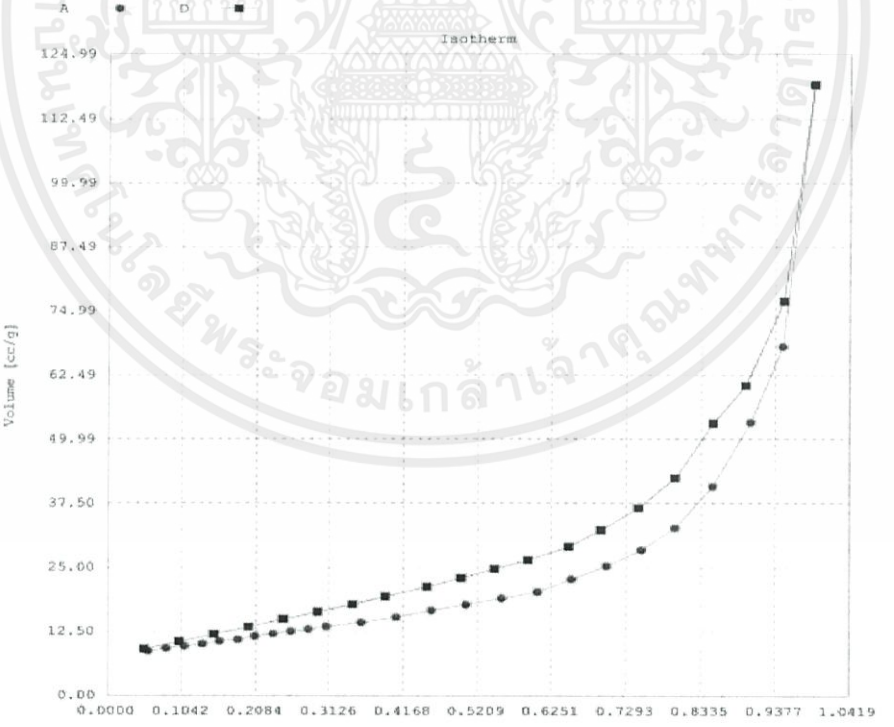

Figure B12. Isotherm of $Ce_{0.8}Co_{0.2}O_2$ calcined at 450°C 2.5h

APPENDIX C

RAMAN SPECTROSCOPY

Table C1. Summary of the position of bands and the corresponding FWHMs.

Catalyst		Peak position (cm^{-1})	Full width at half maximum (cm^{-1})
CeO_2 (HSA)	As-made	460	24.34
	Calcined	461	24.18
$Ce_{0.8}Zr_{0.2}O_2$	As-made	461	24.35
	Calcined	463	22.49
$Ce_{0.5}Zr_{0.5}O_2$	As-made	463	35.81
	Calcined	466	39.93
$Ce_{0.8}Cu_{0.2}O_2$	As-made	447	37.76
	Calcined	447	39.31
$Ce_{0.8}Co_{0.2}O_2$	As-made	446	45.16
	Calcined	450	45.63

APPENDIX D

TGA

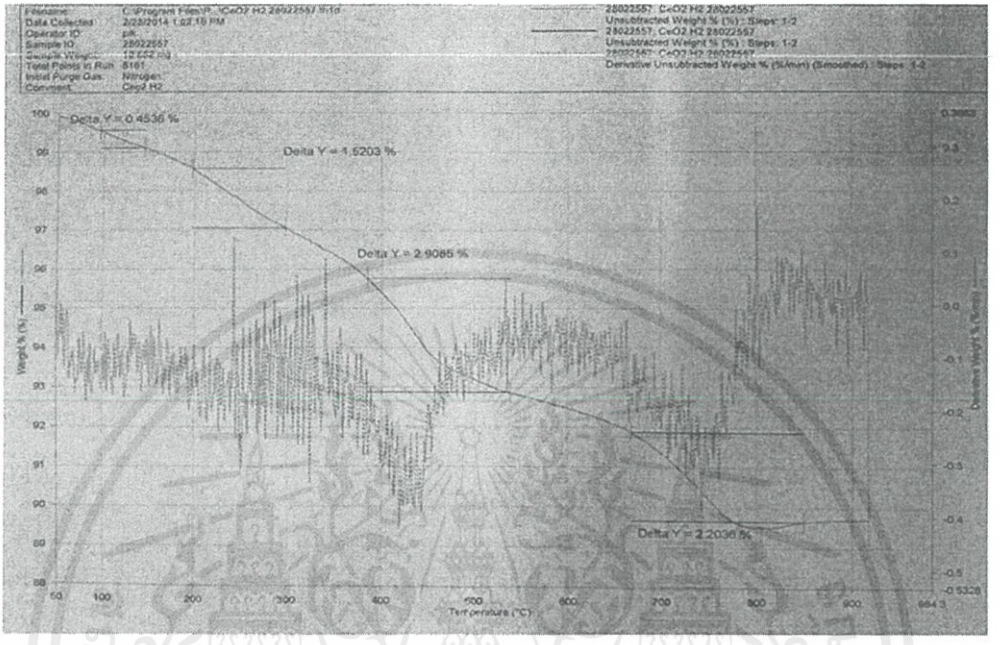

Figure D1 TGA of reduced ceria (HSA) with hydrogen carrier gas

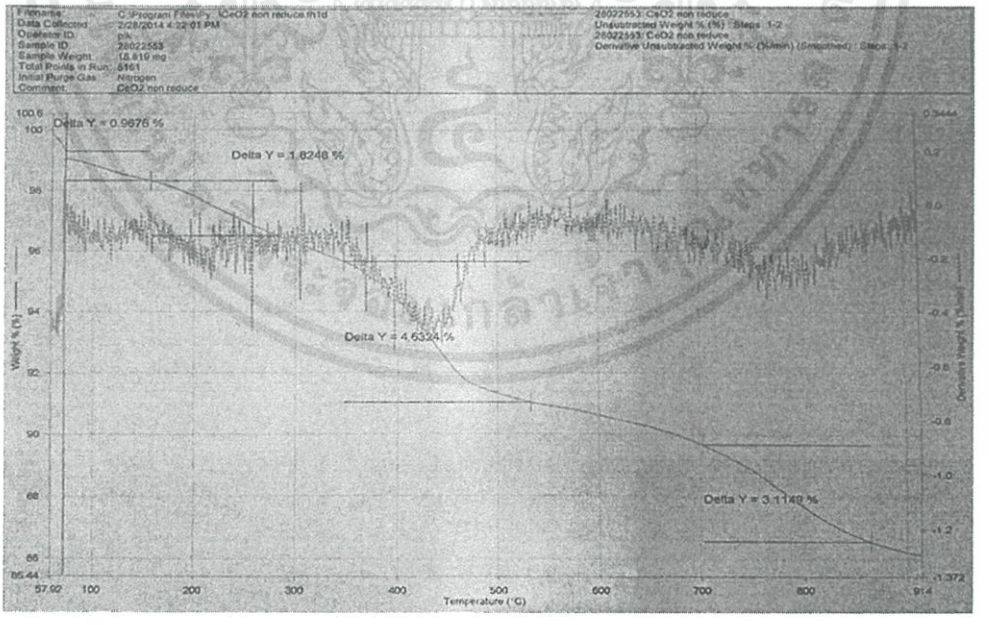

Figure D2 TGA of non-reduced ceria (HSA) with nitrogen carrier gas

APPENDIX E

CALCULATION

Calculations of catalytic parameters

Contact time (W/F)

$$\frac{W}{F} = \frac{weight\ of\ catalyst\ (g)}{Mole\ of\ reactant\ (\frac{mol}{h})}$$

In a reaction employing 0.000248 mol/h of palmitic acid in feed and with 0.1987 grams of a catalyst, the W/F is calculated as follows:

$$\frac{W}{F} = \frac{0.1987\ (g)}{0.000248\left(\frac{mol}{h}\right)}$$
$$= 800\ \text{g. h/mol}$$

Calculation of %yield from gas chromatography

From the chromatogram, the peaks of hydrocarbon samples were identified by comparing with the reference standard. The peak area of hydrocarbon products (including oxygenated compounds) which possess the equal number of carbon was summarized in **Table E1**.

Table E1.The summation of the peak area for hydrocarbon products.

Number of carbon	Peak area	Corrected peak area
C_9	2,453,160	272,573
C_{10}	1,640,424	164,042
C_{11}	1,237,542	112,504
C_{12}	1,053,018	87,752
C_{13}	1,548,791	119,138
C_{14}	2,903,115	207,365
C_{15}	2,903,115	386,480
C_{16}	5,797,196	77,198
2-Heptadecanone	17,769,500	1,269,250
Total	35,637,772	2,696,293

$$Corrected\ peak\ area\ in\ each\ product = \frac{Corrected\ peak\ area\ of\ C_n \times 100}{Total\ corrected\ area}$$

Each peak was corrected by a response factor (RF) which is considered to be equivalent to the carbon number. For example,

$$Corrected\ peak\ area\ of\ C_9 = \frac{2,453,160}{9} = 272,573$$

In the normalization method, the areas of all eluted peak were computed after correcting these areas for the difference in the detector response for different types of compounds. After the correction, the concentration of the analyzed species can be calculated from the ratio of its areas to the total area of all peaks. Percent yield of each component in a sample as follows:

$$\%\ \text{Yield in each product} = \frac{corrected\ peak\ area\ of\ C_n \times 100}{Total\ corrected\ area}$$

For example;

$$\%\ \text{Yield of } C_9 = \frac{272,573 \times 100}{2,696,293}$$

The percent carbon yield of each sample as obtained from the above calculation is shown in **Table E2.**

Table E2 %Carbon yield derived by normalization method.

Number of carbon	% Yield of sample
C_9	10.1
C_{10}	6.1
C_{11}	4.2
C_{12}	3.3
C_{13}	4.4
C_{14}	7.7
C_{15}	14.3
C_{16}	2.9
Palmitic acid	47.1
Total	100

The conversion of palmitic acid can be calculated by

$$\%\ \text{Conversion} = 100 - (\%\text{Yield of palmitic acid left in product})$$

For example;

$$\%\ \text{Conversion} = 100 - 47.1 = 52.9\ \%$$

APPENDIX F

GAS CHROMATOGRAM

Analysis gas product from gas chromatography

Prior analysis, the structure of products in sample is identified by GC-MS (gas chromatography with mass spectrometer detector). Then, the quantitative analysis of products was carried by GC-FID (gas chromatography with flam ionization detector) with the condition expressed in **Table F1**.

Table F1 The GC condition for quantitative analysis.

Column	HP-5 (30 m x 0.25 mm x 0.025 μm)
Temperature program	40°C (10 min hold) to 280°C (60 min hold) at 15°C/min
Carrier gas	Nitrogen gas
Injector temperature	265 °C
Detector temperature	FID at 280°C

Table F2 Chromatogram data of standard product distribution and feed.

Products or feed	Retention time of standard (min)	Products or feed	Retention time of standard (min)
C9 unsat	13.982	C14 sat	19.678
C9 sat	14.141	C15 unsat	20.415
C10 unsat	15.592	C15 sat	20.468
C10 sat	15.703	C16 unsat	21.168
C11 unsat	16.813	C16 sat	21.245
C11 sat	16.902	C17 unsat	21.843
C12 unsat	17.845	C17 sat	21.912
C12 sat	17.902	C17 ketone	22.660
C13 unsat	18.763	Palmitic acid	23.0
C13 sat	18.883	C31 ketone	33.853
C14 unsat	19.618		

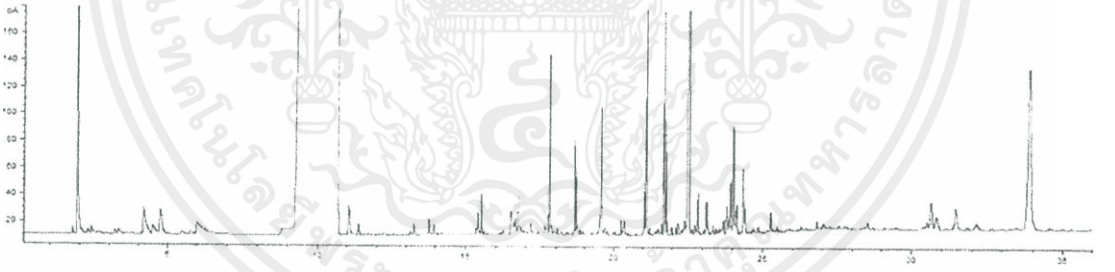

Figure F1 The GC chromatogram of ketonization of palmitic acid.

APPENDIX G

REACTION DATA

1. Reduced ceria (HSA) under H_2 flow

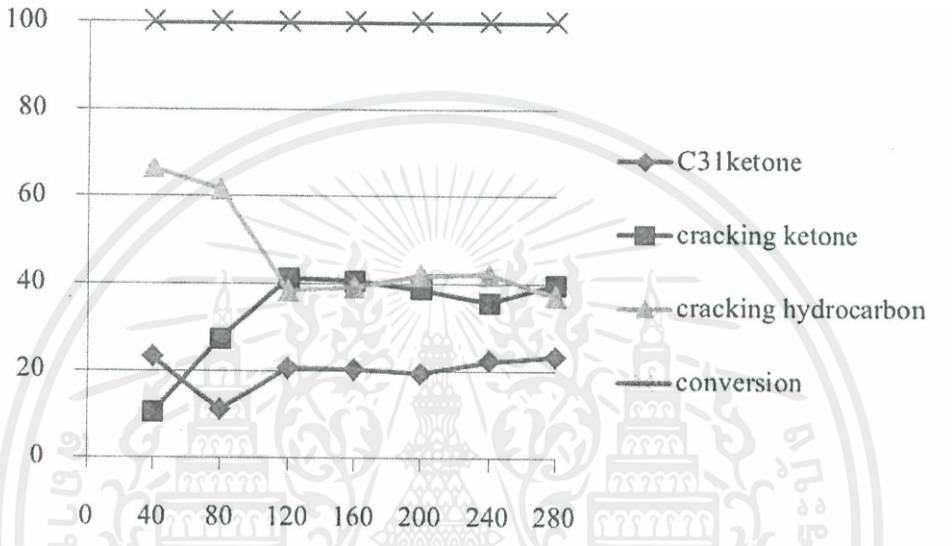

Figure G1 Conversion of palmitic acid and yield of products in reduced ceria (HSA) / H_2 flow

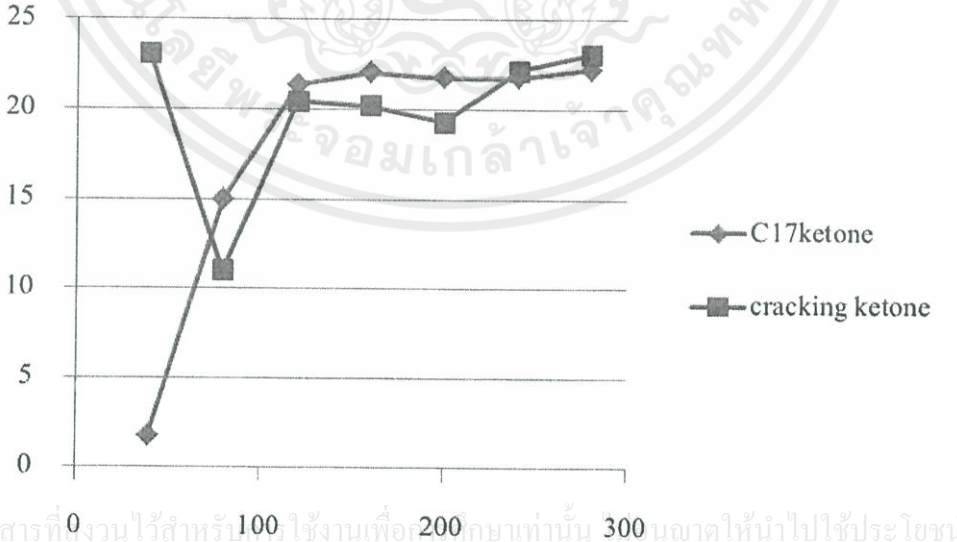

Figure G2 Yield of cracking ketone & alcohol products in reduced ceria (HSA) / H_2 flow

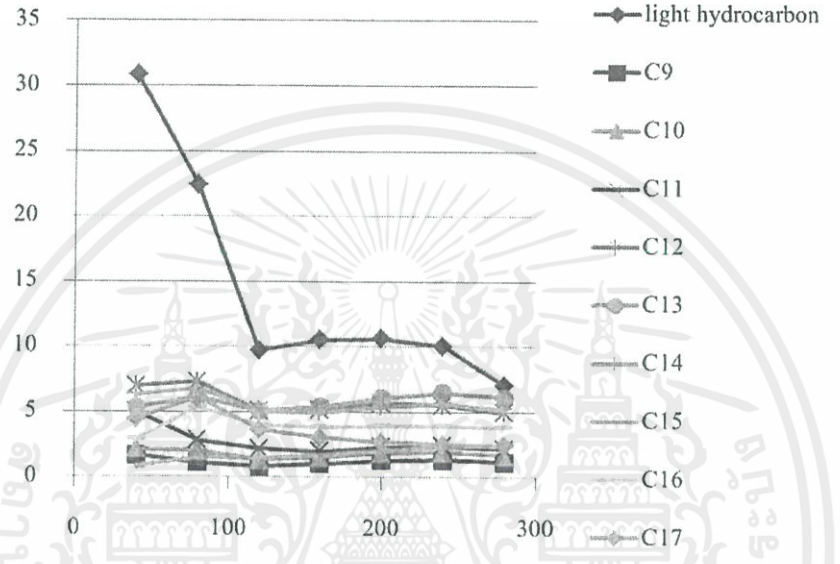

Figure G3 Yield of cracking hydrocarbons product in reduced ceria (HSA) / H_2 flow

2. Reduced ceria (HSA) under N_2 flow

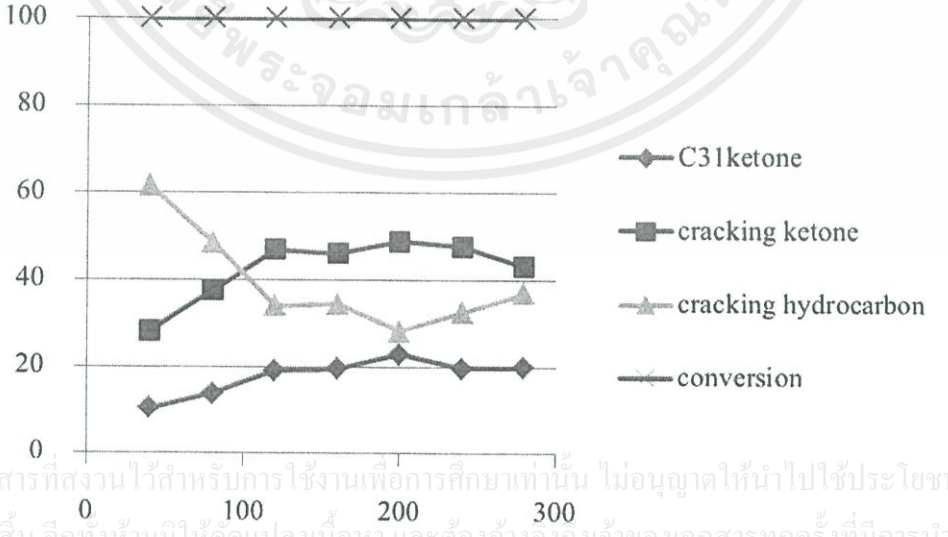

Figure G4 Conversion of palmitic acid and yield of products in reduced ceria (HSA) / N_2 flow

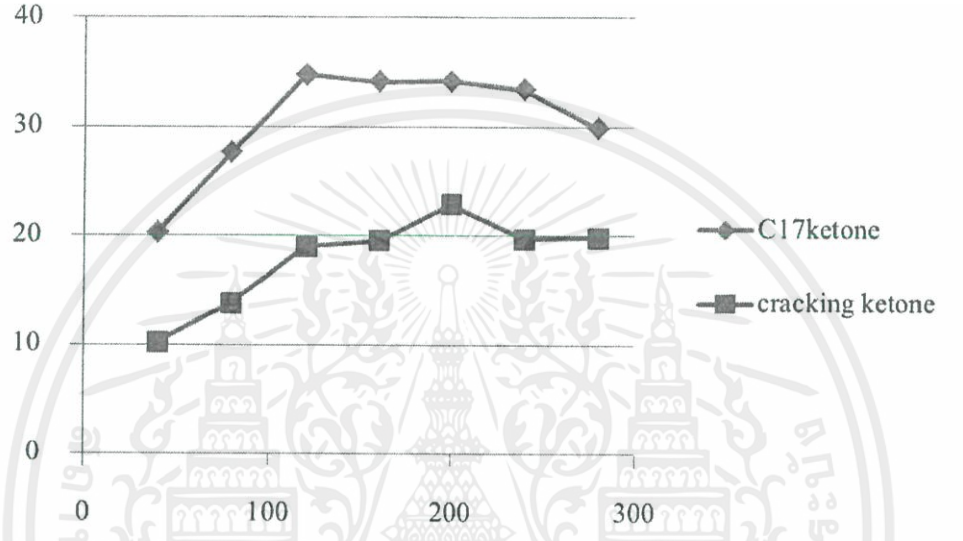

Figure G5 Yield of cracking ketone & alcohol products in reduced ceria (HSA) / N_2 flow

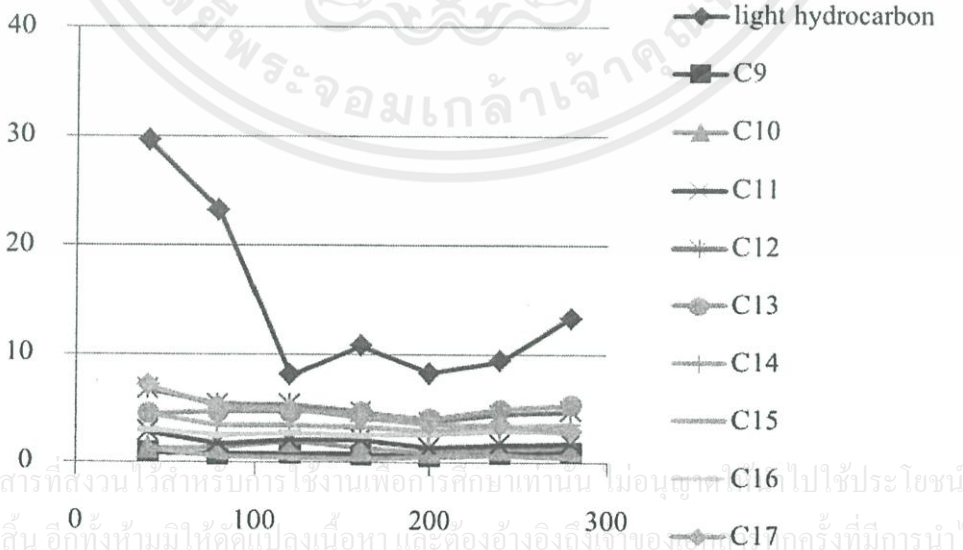

Figure G6 Yield of cracking hydrocarbons product in reduced ceria (HSA) / N_2 flow

3. Non-reduced ceria (HSA) under N_2 flow

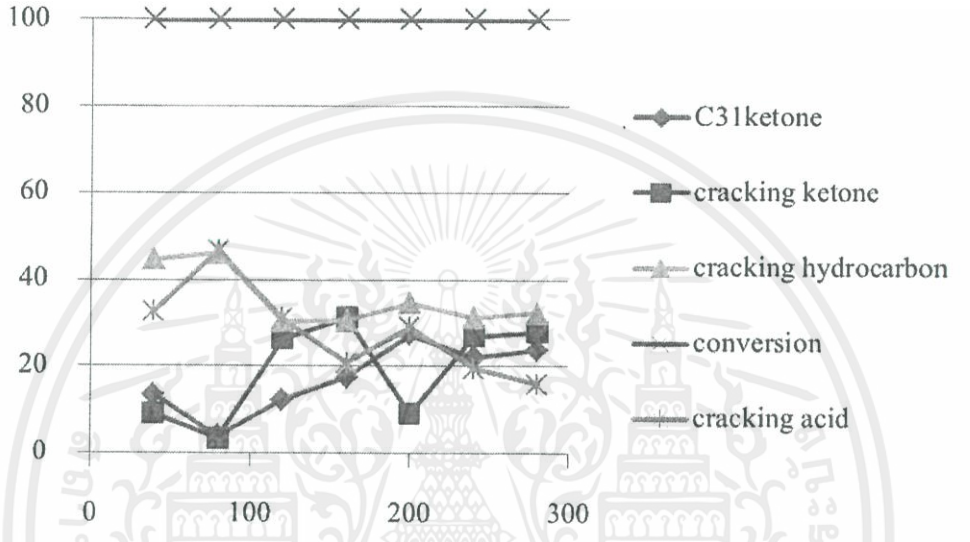

Figure G7 Conversion of palmitic acid and yield of products in non-reduced ceria (HSA) / N_2 flow

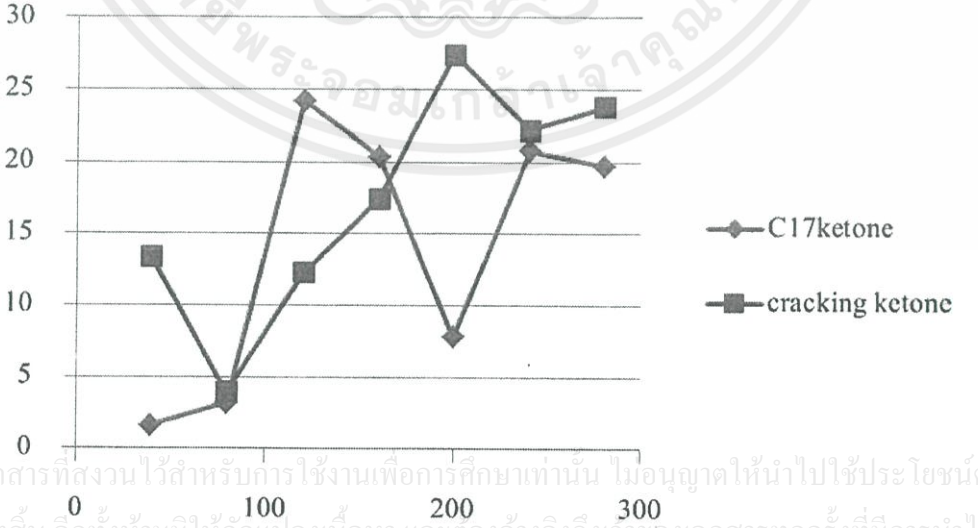

Figure G8 Yield of cracking ketone & alcohol products in non-reduced ceria (HSA) / N_2 flow

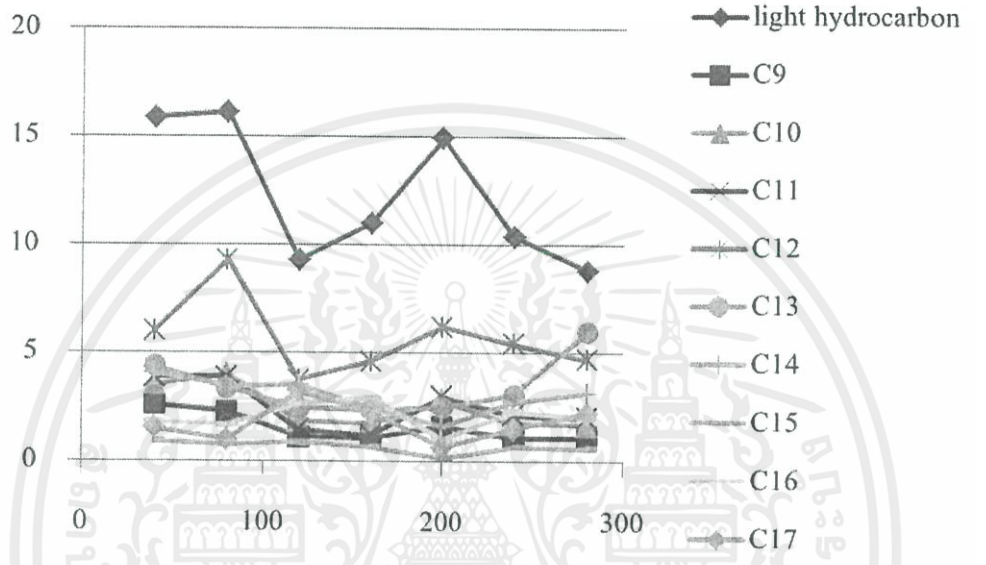

Figure G9 Yield of cracking hydrocarbons product in non-reduced ceria (HSA) / N_2 flow

4. Reduced ceria (LSA) under N_2 flow

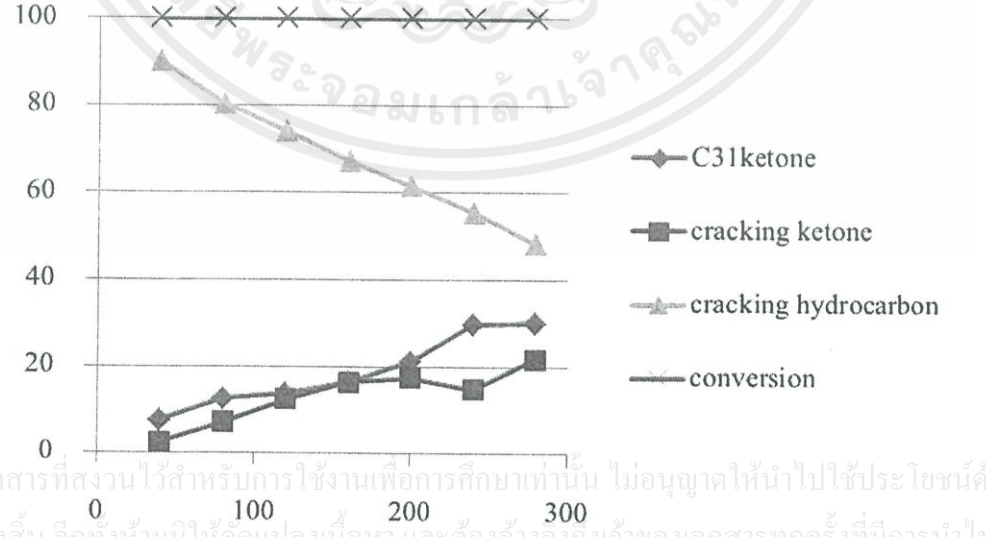

Figure G10 Conversion of palmitic acid and yield of products in reduced ceria (LSA) / N_2 flow

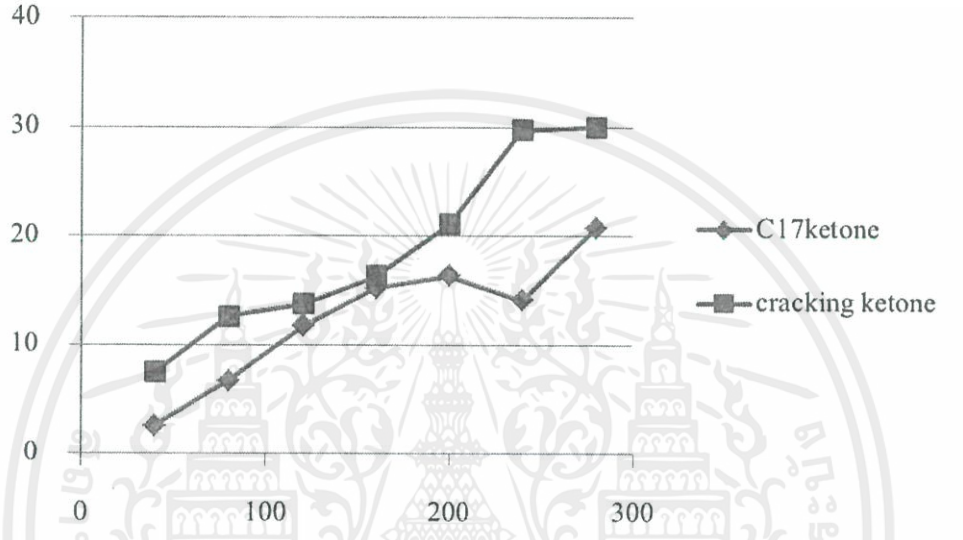

Figure G11 Yield of cracking ketone & alcohol products in reduced ceria (LSA) / N_2 flow

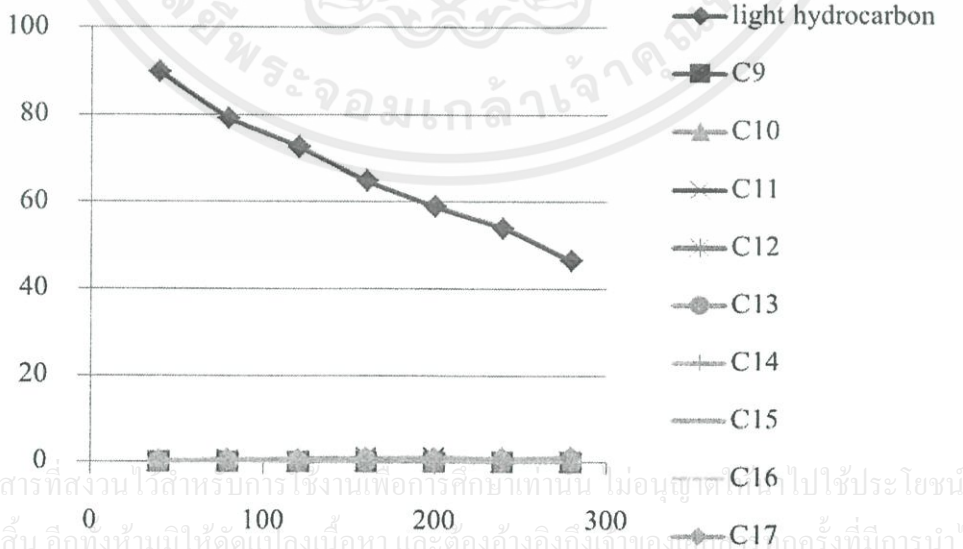

Figure G12 Yield of cracking hydrocarbons product in reduced ceria (LSA) / N_2 flow

5. Reduced $Ce_{0.8}Cu_{0.2}O_2$ under N_2 flow

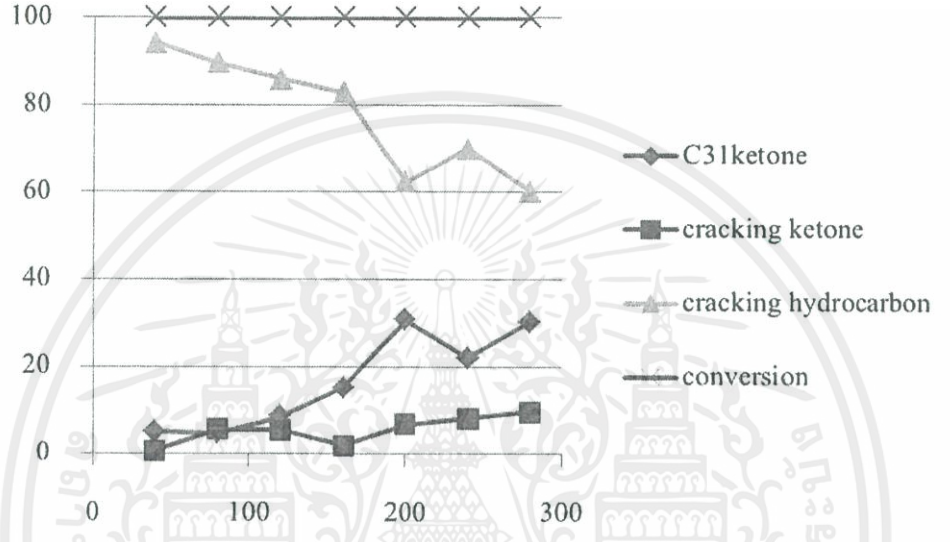

Figure G13 Conversion of palmitic acid and yield of products in reduced $Ce_{0.8}Cu_{0.2}O_2$ / N_2 flow

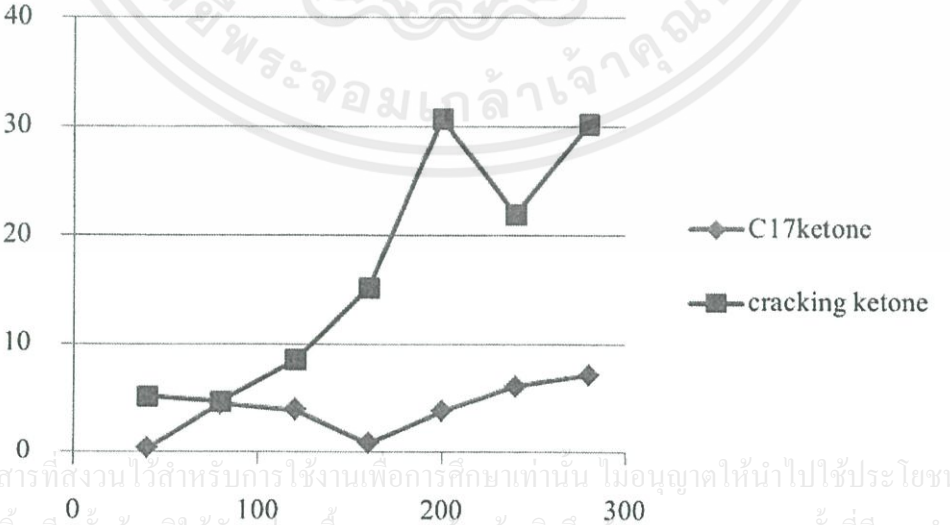

Figure G14 Yield of cracking ketone & alcohol products in reduced $Ce_{0.8}Cu_{0.2}O_2$ / N_2 flow

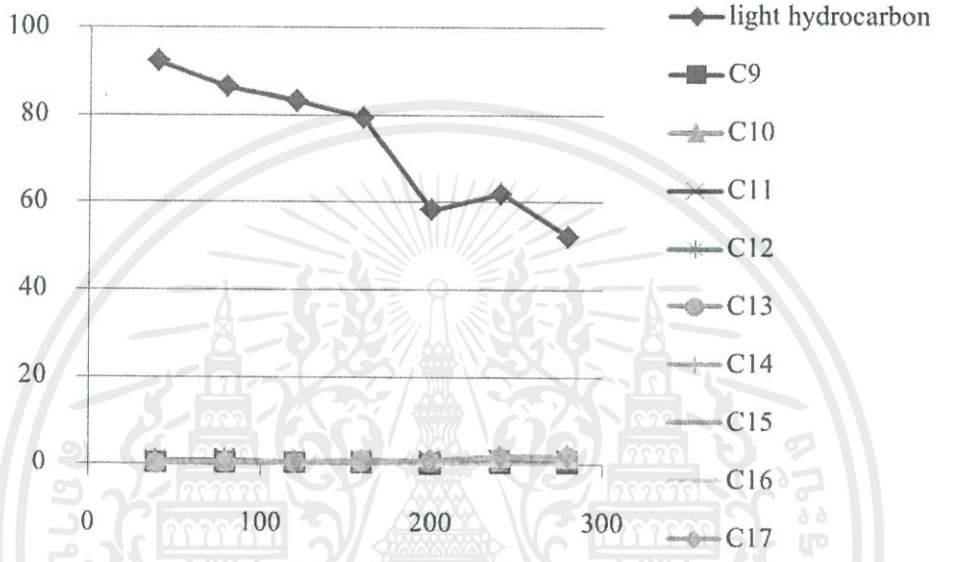

Figure G15 Yield of cracking hydrocarbons product in reduced $Ce_{0.8}Cu_{0.2}O_2$ / N_2 flow

6. Reduced $Ce_{0.8}Co_{0.2}O_2$ under N_2 flow

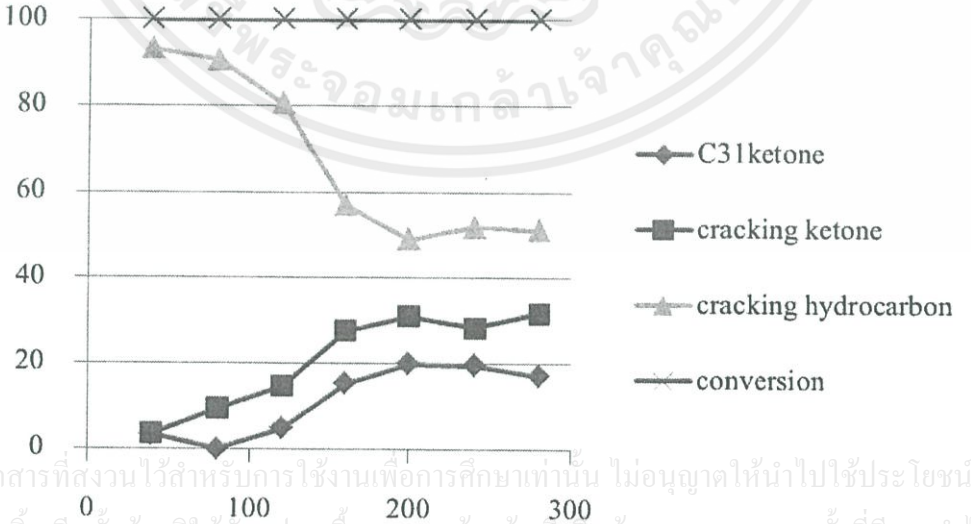

Figure G16 Conversion of palmitic acid and yield of products in reduced $Ce_{0.8}Co_{0.2}O_2$ / N_2 flow

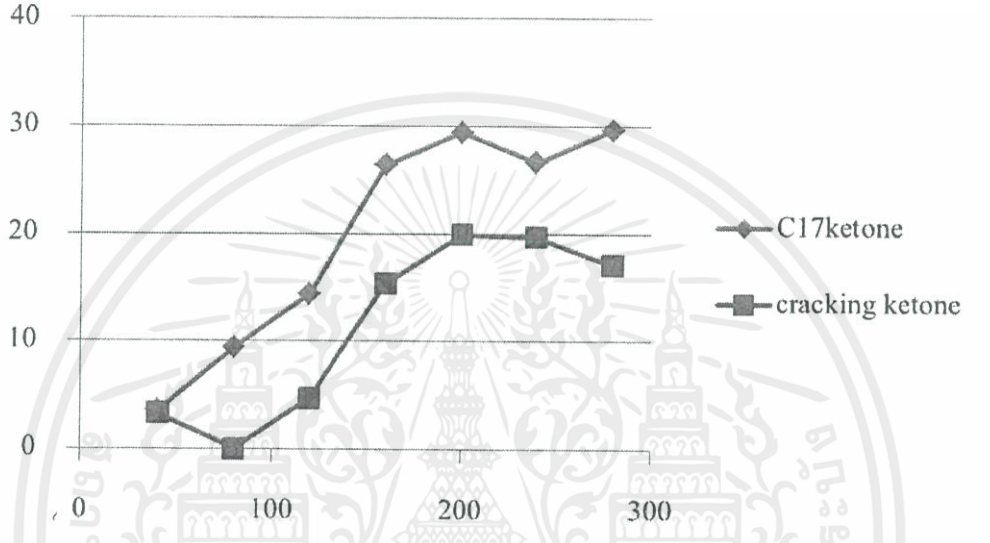

Figure G17 Yield of cracking ketone & alcohol products in reduced $Ce_{0.8}Co_{0.2}O_2$ / N_2 flow

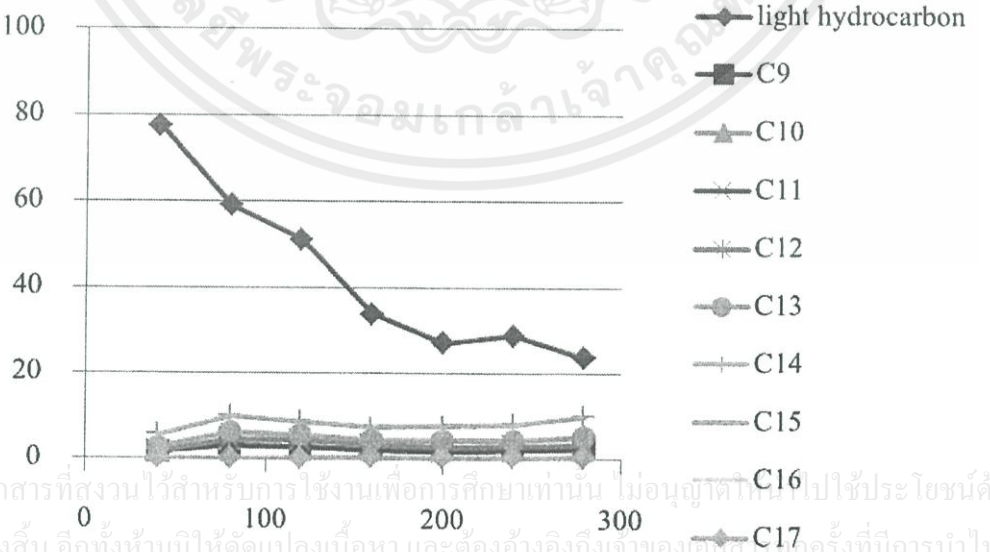

Figure G18 Yield of cracking hydrocarbons product in reduced $Ce_{0.8}Co_{0.2}O_2$ / N_2 flow

7. Reduced $Ce_{0.8}Zr_{0.2}O_2$ under N_2 flow

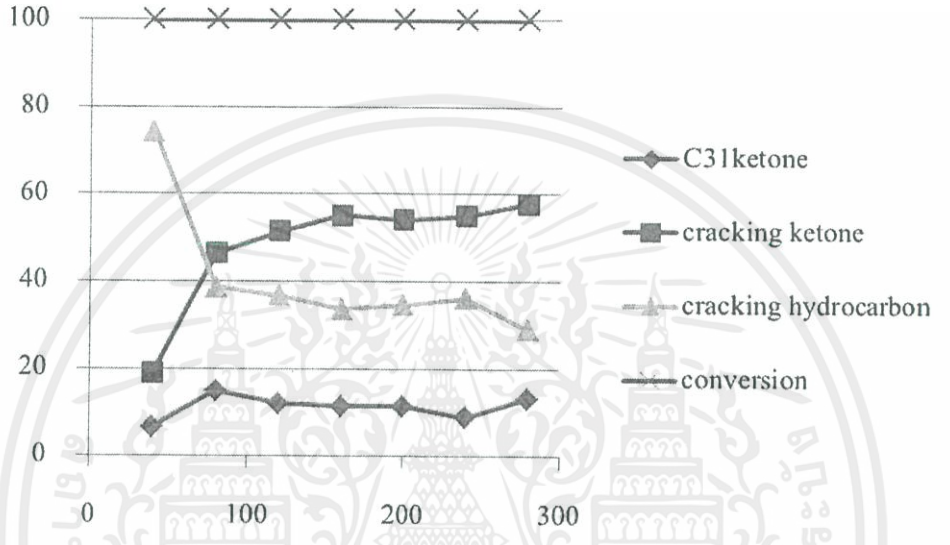

Figure G19 Conversion of palmitic acid and yield of products in reduced $Ce_{0.8}Zr_{0.2}O_2$ / N_2 flow

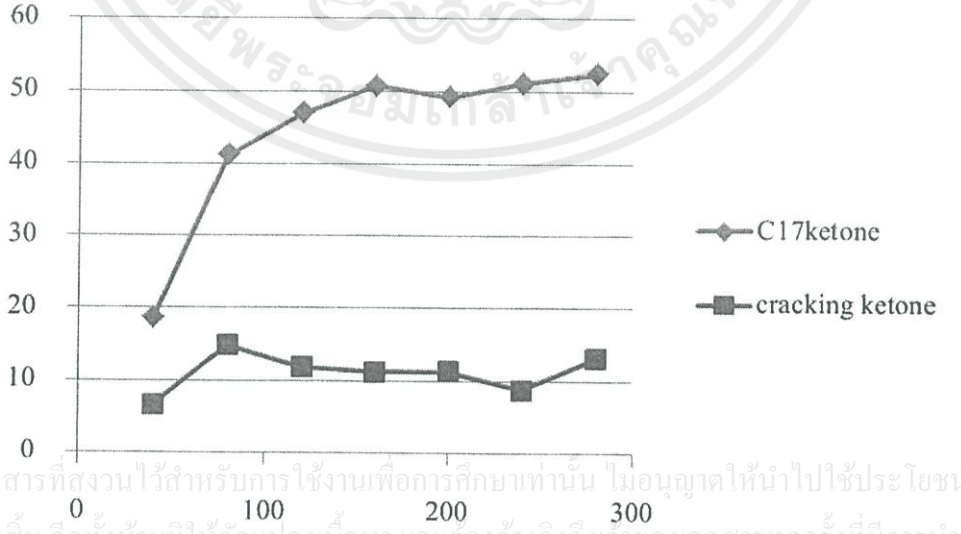

Figure G20 Yield of cracking ketone & alcohol products in reduced $Ce_{0.8}Zr_{0.2}O_2$ / N_2 flow

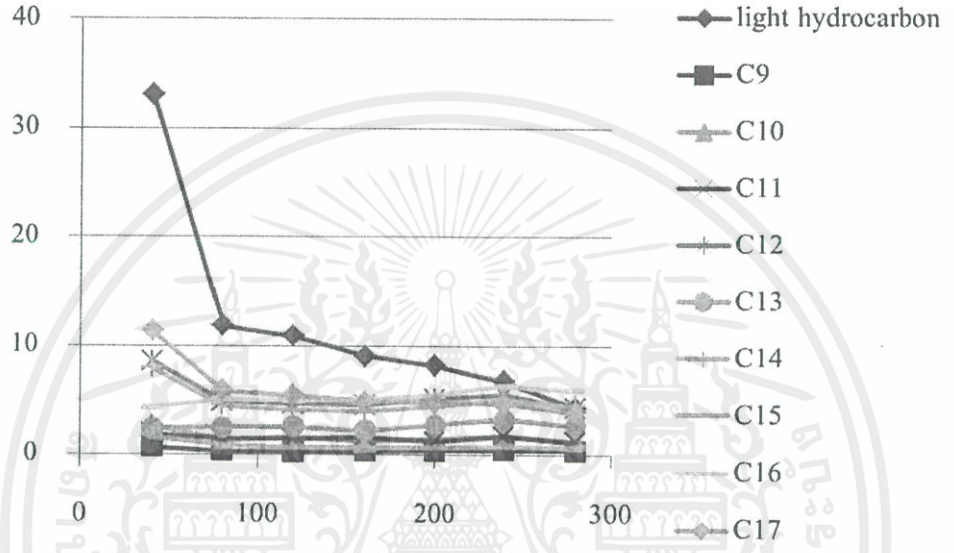

Figure G21 Yield of cracking hydrocarbons product in reduced $Ce_{0.8}Zr_{0.2}O_2$ / N_2 flow

8. Reduced $Ce_{0.5}Zr_{0.5}O_2$ under N_2 flow

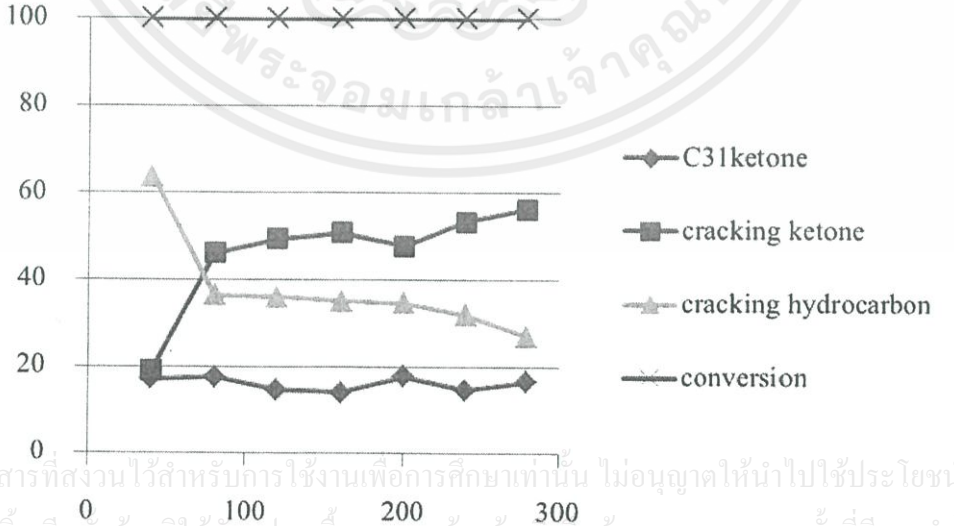

Figure G22 Conversion of palmitic acid and yield of products in reduced $Ce_{0.5}Zr_{0.5}O_2$ / N_2 flow

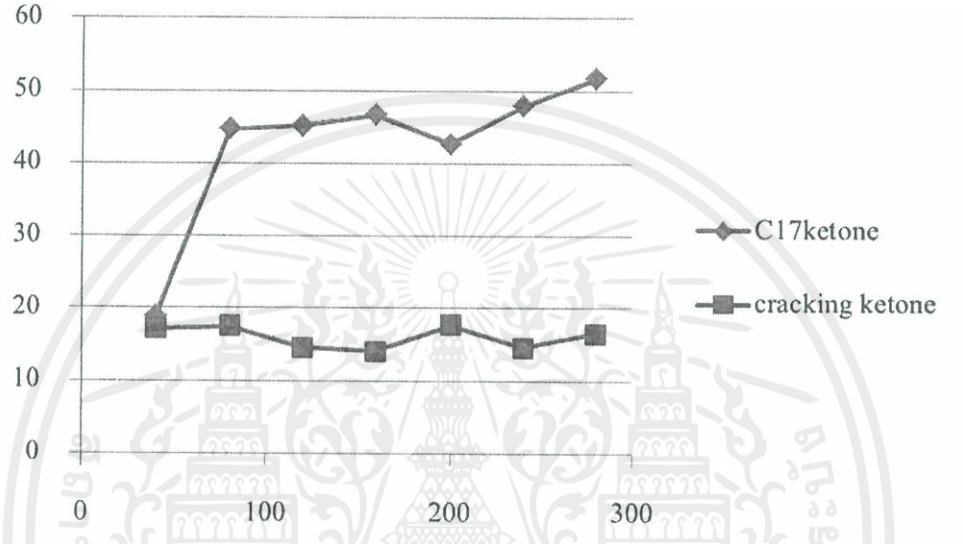

Figure G23 Yield of cracking ketone & alcohol products in reduced $Ce_{0.5}Zr_{0.5}O_2$ / N_2 flow

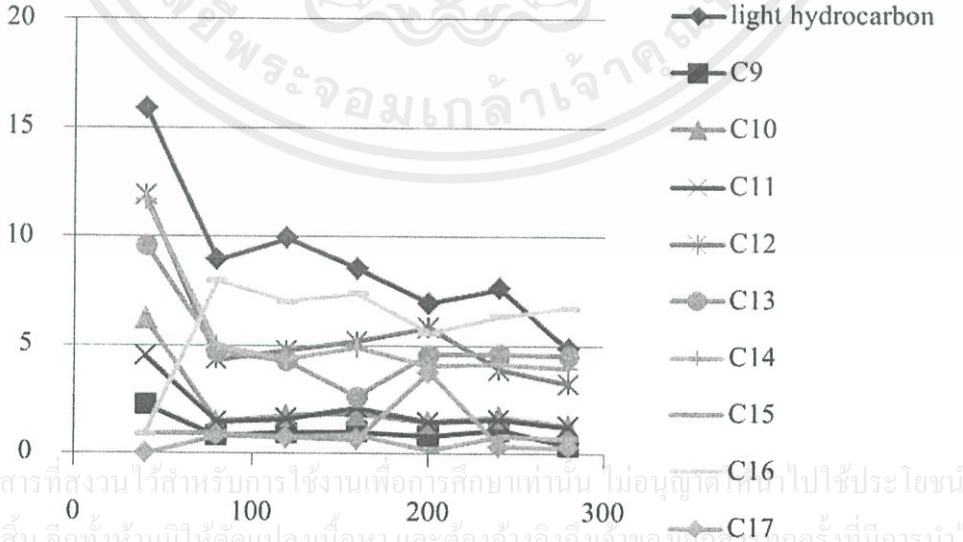

Figure G24 Yield of cracking hydrocarbons product in reduced $Ce_{0.5}Zr_{0.5}O_2$ / N_2 flow